

ROBUST IMAGING WITH ELECTROMAGNETIC WAVES IN NOISY ENVIRONMENTS

LILIANA BORCEA* AND JOSSELIN GARNIER†

Abstract. We study imaging with an array of sensors that probes a medium with single frequency electromagnetic waves and records the scattered electric field. The medium is known and homogenous except for some small and penetrable inclusions. The goal of inversion is to locate and characterize these inclusions from the data collected by the array, which are corrupted by additive noise. We use results from random matrix theory to obtain a robust inversion method. We assess its performance with numerical simulations and quantify the benefit of measuring more than one component of the scattered electric field.

Key words. imaging, electromagnetic waves, random matrix theory.

1. Introduction. We study an inverse problem for Maxwell's equations, where unknown scatterers in a medium are to be determined from data collected with an array of sources and receivers. The sources emit signals which propagate in the medium and the receivers record the backscattered waves. The recordings, indexed by the source and receiver pair, are the entries in the response matrix, the data, which are contaminated with additive noise.

Sensor array imaging is an important technology in nondestructive testing, medical imaging, radar, seismic exploration, and elsewhere. It operates over application specific ranges of frequencies and fixed or synthetic apertures. We consider imaging with single frequency waves and a fixed array of N sensors that play the dual role of sources and receivers. The unknown scatterers lie in a homogeneous medium. They are P penetrable inclusions of small size with respect to the wavelength. As shown in [5] they can be described by their center location \vec{y}_p and reflectivity tensor ρ_p which depends on the volume and shape of their support, and their electric permittivity ϵ_p , for $p = 1, \dots, P$.

There are many algorithms for locating scatterers from the response matrix. Reverse time or Kirchhoff migration [11] and the similar filtered backprojection [14] are common in seismic and radar imaging with broadband data. Matched field processing [7] is popular in underwater acoustics. Qualitative methods such as linear sampling [12], the factorization method [20], and the MUSIC (Multiple Signal Classification) algorithm [22] are useful for imaging with single frequency waves, and give high resolution results if the noise is weak.

A study of noise effects on the MUSIC method can be found in [16]. It determines upper bounds on the noise level that guarantee the exact recovery of point scatterers in a sparse scene. Here we consider stronger noise and use results from random matrix theory [10, 13, 8, 21] to obtain a robust MUSIC type localization method. Such results have led to scatterer detection tests in [3, 4], and to filters of backscattered waves in random media in [6, 1]. They are also the foundation of a robust sonar array imaging method of well separated point scatterers in [17]. We extend the results in [17] to electromagnetic waves, for locating one or more inclusions and estimating their reflectivity tensor. We also quantify the benefits of measuring more than one component of the scattered electric field.

*Department of Mathematics, University of Michigan, Ann Arbor, MI 48109. borcea@umich.edu

†Laboratoire de Probabilités et Modèles Aléatoires & Laboratoire Jacques-Louis Lions, Université Paris Diderot, 75205 Paris Cedex 13, France. garnier@math.univ-paris-diderot.fr

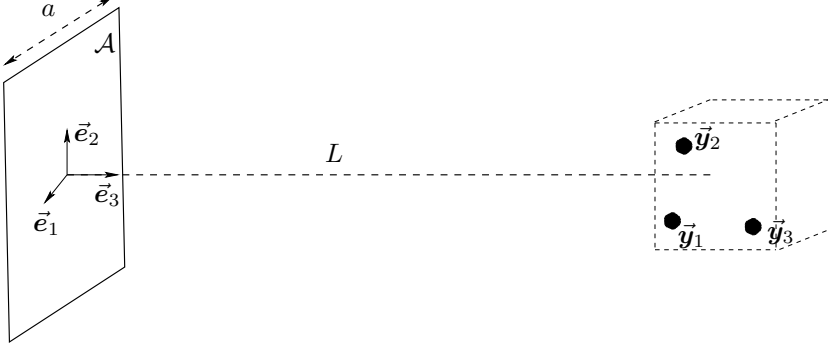


FIG. 2.1. *Illustration of the inversion setup. The array \mathcal{A} is square planar with side a , in the cross-range plane spanned by \vec{e}_1 and \vec{e}_2 . The imaging region is at range scale L from the array. In the illustration there are three inclusions at locations \vec{y}_p , for $p = 1, 2, 3$.*

The paper is organized as follows: We begin in section 2 with the mathematical formulation of the inverse problem, and then give in section 3 the data model. The singular value decomposition analysis of the response matrix is described in section 4. The inversion method uses this analysis and is presented in section 5. Numerical simulation results are shown in section 6. We end with a summary in section 7.

2. Formulation of the problem. Consider a homogeneous isotropic medium with electric permittivity ϵ_o and magnetic permeability μ_o , which contains P penetrable inclusions supported in the disjoint simply connected domains Ω_p with smooth boundaries, centered at locations \vec{y}_p , for $p = 1, \dots, P$. The inclusions are modelled by the piecewise constant electric permittivity

$$\epsilon(\vec{x}) = \sum_{p=1}^P \epsilon_p 1_{\Omega_p}(\vec{x}) + \epsilon_o 1_{\mathbb{R}^3 \setminus \Omega}(\vec{x}), \quad \Omega = \bigcup_{p=1}^P \Omega_p, \quad (2.1)$$

where $1_{\Omega}(\vec{x})$ is the indicator function of the domain Ω , and ϵ_p are scalar real valued for $p = 1, \dots, P$.

The medium is probed with N sensors that are both sources and receivers. They are closely spaced at locations $\{\vec{x}_r\}_{1 \leq r \leq N}$ in a set \mathcal{A} , so they behave like a collective entity, the array. For convenience we let \mathcal{A} be planar and square, of side a , the array aperture. This allows us to introduce a system of coordinates with origin at the center of the array and orthonormal basis $\{\vec{e}_1, \vec{e}_2, \vec{e}_3\}$. The vectors \vec{e}_1, \vec{e}_2 span the plane of the array, named the cross-range plane, and the line along \vec{e}_3 is the range direction. The distance between the array and the inclusions is of order L , the range scale. See Figure 2.1 for an illustration.

We index consistently a source sensor by s and a receiver sensor by r , although both s and r take values in the same set $\{1, \dots, N\}$. The sources are point dipoles with current density $\vec{j}_s \delta(\vec{x} - \vec{x}_s)$, and the resulting electric field \vec{E} satisfies

$$\vec{\nabla} \times \vec{\nabla} \times \vec{E}(\vec{x}; \vec{x}_s) - k^2 \frac{\epsilon(\vec{x})}{\epsilon_o} \vec{E}(\vec{x}; \vec{x}_s) = ik \sqrt{\frac{\mu_o}{\epsilon_o}} \vec{j}_s \delta(\vec{x} - \vec{x}_s), \quad (2.2)$$

and the radiation condition

$$\lim_{|\vec{x}| \rightarrow \infty} |\vec{x}| \left[\vec{\nabla} \times \vec{E}(\vec{x}; \vec{x}_s) - ik \frac{\vec{x}}{|\vec{x}|} \times \vec{E}(\vec{x}; \vec{x}_s) \right] = 0. \quad (2.3)$$

Equation (2.3) is derived from Maxwell's equations at frequency ω , and

$$k = \frac{\omega}{c_o} = \frac{2\pi}{\lambda}$$

is the wavenumber, where $c_o = 1/\sqrt{\mu_o\epsilon_o}$ is the wave speed and λ is the wavelength.

We decompose \vec{E} in the direct field \vec{E}_o and the scattered one denoted by $\vec{\mathcal{E}}$,

$$\vec{\mathcal{E}}(\vec{x}; \vec{x}_s) = \vec{E}(\vec{x}; \vec{x}_s) - \vec{E}_o(\vec{x}; \vec{x}_s). \quad (2.4)$$

The direct field solves the analogue of (2.2)–(2.3) in the homogeneous medium, and can be written explicitly as

$$\vec{E}_o(\vec{x}; \vec{x}_s) = ik\sqrt{\frac{\mu_o}{\epsilon_o}} \mathbf{G}(\vec{x}, \vec{x}_s) \vec{j}_s, \quad (2.5)$$

using the dyadic Green's tensor

$$\mathbf{G}(\vec{x}, \vec{z}) = \left(\mathbf{I}_3 + \frac{\nabla \nabla^T}{k^2} \right) \frac{e^{ik|\vec{x}-\vec{z}|}}{4\pi|\vec{x}-\vec{z}|}. \quad (2.6)$$

The scattered field $\vec{\mathcal{E}}$ is recorded at the N receivers, and the experiment may be repeated by emitting waves sequentially from all the sources. Each source may use up to three illuminations, with linearly independent $\vec{j}_s \in \mathbb{R}^3$, and the receivers may record one or all three components of $\vec{\mathcal{E}}$. We call the data for all possible illuminations and recordings *complete*. All other cases, with one or two illuminations from each source and one or two components of $\vec{\mathcal{E}}$ measured at the receivers are called *incomplete*. The goal is to locate and characterize the inclusions using the complete or incomplete measurements.

We simplify the problem by assuming that the inclusions are small with respect to the wavelength, so we can represent them as in [5] by their center locations \vec{y}_p and 3×3 reflectivity tensors ρ_p , for $p = 1, \dots, P$. These tensors depend on the shape of the domains Ω_p and the relative electric permittivity ϵ_p/ϵ_o . The inverse problem is to determine the locations \vec{y}_p and reflectivity tensors ρ_p from the array measurements.

3. Data model. Let α be a small and positive dimensionless parameter which scales the size of the inclusions

$$\frac{[\text{Vol}(\Omega_p)]^{1/3}}{\lambda} \sim \alpha \ll 1, \quad p = 1, \dots, P, \quad (3.1)$$

and denote by $\vec{\mathcal{E}}_q(\vec{x}; \vec{x}_s)$ the scattered field due to the source at \vec{x}_s , with $\vec{j}_s = \vec{e}_q$. It has the following asymptotic expansion in the limit $\alpha \rightarrow 0$, as shown in [5],

$$\vec{\mathcal{E}}_q(\vec{x}; \vec{x}_s) = ik^3 \sqrt{\frac{\mu_o}{\epsilon_o}} \sum_{p=1}^P \mathbf{G}(\vec{x}, \vec{y}_p) \rho_p \mathbf{G}(\vec{y}_p, \vec{x}_s) \vec{e}_q + O(\alpha^4). \quad (3.2)$$

The reflectivity tensor of the m -th inclusion is defined by

$$\rho_p = \alpha^3 \left(\frac{\epsilon_p}{\epsilon_o} - 1 \right) \mathbf{M}_p, \quad (3.3)$$

using the α -independent polarization tensor \mathbf{M}_p . We refer to [5] for details on \mathbf{M}_p , and to section 6 for its calculation in our numerical simulations. It suffices to say that \mathbf{M}_p is a symmetric, real valued 3×3 matrix which depends on the shape of Ω_p and the relative electric permittivity ϵ_p/ϵ_o .

3.1. The noiseless data model. Since k , μ_o and ϵ_o are known, let us model the noiseless data gathered with the receiver and source pair (r, s) by

$$\mathbf{d}(\vec{x}_r, \vec{x}_s) = \frac{\sqrt{\epsilon_o/\mu_o}}{ik^3} \left(\vec{\mathcal{E}}_1, \vec{\mathcal{E}}_2, \vec{\mathcal{E}}_3 \right), \quad r, s = 1, \dots, N. \quad (3.4)$$

This is a 3×3 complex matrix, the (r, s) block of the $3N \times 3N$ *complete data matrix* \mathbf{D} collected by the array,

$$\mathbf{D} = (\mathbf{d}(\vec{x}_r, \vec{x}_s))_{r,s=1,\dots,N}. \quad (3.5)$$

To acquire \mathbf{D} directly, the array would use the sources sequentially, with current densities $\vec{e}_q \delta(\vec{x} - \vec{x}_s)$, for $q = 1, 2, 3$ and $s = 1, \dots, N$, and would measure the scattered fields $\vec{\mathcal{E}}_q(\vec{x}; \vec{x}_s)$ at the receivers. This acquisition method is not optimal in noisy environments, and may be improved as explained in the next section.

When the sensors emit and receive only along one or two directions, we have incomplete measurements. Let us denote by $\mathcal{S} \subset \{1, 2, 3\}$ the set of indices of the measured components of the electric field, and define the $3 \times |\mathcal{S}|$ *sensing matrix*

$$\mathbf{S} = (\vec{e}_q)_{q \in \mathcal{S}}, \quad (3.6)$$

with columns given by the unit vectors \vec{e}_q with $q \in \mathcal{S}$. We assume for convenience that the source excitation currents are also limited to these directions, and denote the incomplete data matrix by \mathbf{D}_s . It is a complex $|\mathcal{S}|N \times |\mathcal{S}|N$ matrix that can be written in terms of \mathbf{D} as

$$\mathbf{D}_s = \text{diag}(\mathbf{S}^T, \dots, \mathbf{S}^T) \mathbf{D} \text{diag}(\mathbf{S}, \dots, \mathbf{S}). \quad (3.7)$$

The mathematical model of \mathbf{D} follows from (3.2) and (3.4). We write it using the forward map \mathcal{F} , which takes the unknown locations and reflectivity tensors of the inclusions to the space $\mathbb{C}^{3N \times 3N}$ of matrices where \mathbf{D} lies,

$$\mathbf{D} \approx \mathcal{F}(\vec{y}_1, \dots, \vec{y}_P, \rho_1, \dots, \rho_P) = \left(\sum_{p=1}^P \mathbf{G}(\vec{x}_r, \vec{y}_p) \rho_p \mathbf{G}(\vec{y}_p, \vec{x}_s) \right)_{r,s=1,\dots,N}. \quad (3.8)$$

The forward map for the incomplete measurements is deduced from (3.7)–(3.8). We assume henceforth that \mathcal{F} gives a good approximation of \mathbf{D} , as is the case for sufficiently small α , and treat the approximation in (3.8) as an equality.

3.2. Noisy data and the Hadamard acquisition scheme. In any practical setting the measurements are contaminated with noise, which may be mitigated by the data acquisition scheme, as we now explain.

Suppose that the N sources do not emit waves sequentially, but at the same time, for $3N$ experiments indexed by (n, q) , with $n = 1, \dots, N$ and $q = 1, 2, 3$. In the (n, q) experiment the excitation from the source at \vec{x}_s is $\vec{j}_{s,(n,q)}$, and gathering the measurements for $q = 1, 2, 3$, we obtain the following model of the recordings at the receiver location \vec{x}_r ,

$$\mathbf{d}_{r,n}^H = \sum_{s=1}^N \mathbf{d}(\vec{x}_r, \vec{x}_s) \mathbf{j}_{s,n} + \mathbf{w}_{r,n}. \quad (3.9)$$

This is a 3×3 complex matrix, determined by $\mathbf{d}(\vec{x}_r, \vec{x}_s)$ defined in (3.4), the excitation matrices $\mathbf{j}_{s,n}$ with columns $\vec{j}_{s,(n,q)}$ for $q = 1, 2, 3$, and the noise matrix $\mathbf{w}_{r,n}$. The complete $3N \times 3N$ measurement matrix \mathbf{D}^H has the block structure

$$\mathbf{D}^H = (\mathbf{d}_{r,n}^H)_{r,n=1,\dots,N},$$

and it is modeled by

$$\mathbf{D}^H = \mathbf{D}\mathbf{J} + \mathbf{W}, \quad (3.10)$$

where \mathbf{J} is the excitation matrix with blocks $\mathbf{j}_{s,n}$ for $s, n = 1, \dots, N$, and \mathbf{W} is the noise matrix with blocks $\mathbf{w}_{r,n}$ for $r, n = 1, \dots, N$.

We assume that the excitation currents are normalized so that the entries in \mathbf{J} have unit amplitudes, and take as is usual a noise matrix \mathbf{W} with mean zero and independent complex Gaussian entries with standard deviation σ . This gives

$$\mathbb{E} [\mathbf{W}^\dagger \mathbf{W}] = \sigma^2 \mathbf{I}_{3N},$$

where \dagger denotes the complex conjugate and transpose, \mathbb{E} is the expectation, and \mathbf{I}_{3N} is the $3N \times 3N$ identity matrix. The acquisition scheme uses an invertible \mathbf{J} , to obtain

$$\tilde{\mathbf{D}} = \mathbf{D}^H \mathbf{J}^{-1} = \mathbf{D} + \mathbf{W}, \quad \mathbf{W} = \mathbf{W} \mathbf{J}^{-1}. \quad (3.11)$$

This is a corrupted version of \mathbf{D} , but the noise level in \mathbf{W} , which has mean zero complex Gaussian entries, is reduced for a good choice of \mathbf{J} . Such a choice would give

$$\mathbb{E} [\mathbf{W}^\dagger \mathbf{W}] = (\mathbf{J}^{-1})^\dagger \mathbb{E} [\mathbf{W}^\dagger \mathbf{W}] \mathbf{J}^{-1} = \sigma^2 (\mathbf{J}^{-1})^\dagger \mathbf{J}^{-1} = \sigma_{\mathbf{W}}^2 \mathbf{I}_{3N}, \quad (3.12)$$

and a minimum $\sigma_{\mathbf{W}}$. We conclude that \mathbf{J} must be unitary, up to a multiplicative constant factor, and its determinant should be maximal to get the smallest

$$\sigma_{\mathbf{W}} = \frac{\sigma}{|\det(\mathbf{J})|^{1/(3N)}}.$$

It is shown in [18] that the determinant of $3N \times 3N$ matrices with entries in the complex unit disk is bounded above by $(3N)^{3N/2}$, with equality attained by complex Hadamard matrices. These have entries with modulus one, and are unitary up to the scaling by their determinant. Thus, by using a Hadamard matrix \mathbf{J} , we can mitigate the noise in $\tilde{\mathbf{D}}$ and reduce its standard deviation to

$$\sigma_{\mathbf{W}} = \sigma / \sqrt{3N}. \quad (3.13)$$

The results extend verbatim to the incomplete measurement setup. The difference is that in (3.9) we have $\mathbf{S}^T \mathbf{d}(\vec{x}_r, \vec{x}_s) \mathbf{S}$ instead of $\mathbf{d}(\vec{x}_r, \vec{x}_s)$, and the 3×3 current excitation matrix $\mathbf{j}_{s,n}$ is replaced by $\mathbf{S}^T \mathbf{j}_{s,n} \mathbf{S}$, the blocks in the complex $|\mathcal{S}|N \times |\mathcal{S}|N$ Hadamard matrix. The noise level in

$$\tilde{\mathbf{D}}_s = \mathbf{D}_s + \mathbf{W}_s \quad (3.14)$$

is reduced to $\sigma / \sqrt{|\mathcal{S}|N}$.

Remark: In case that the noise at nearby receivers is correlated, with known correlation structure, let us denote by $\mathbf{C} = \mathbb{E} [\mathbf{W}^\dagger \mathbf{W}]$ the Hermitian covariance matrix, and suppose that it is positive definite, with $O((\sigma^2)^{3N})$ determinant. Then we can use its square root to define an invertible matrix \mathbf{J} so that $\mathbf{C}^{1/2} \mathbf{J}^{-1}$ is unitary up to scaling by its determinant, and obtain that \mathbf{W} in (3.11) has uncorrelated entries with $\sigma_{\mathbf{W}} = O(\sigma / |\det(\mathbf{J})|^{1/(3N)})$.

4. Singular value decomposition analysis. Our imaging algorithm is based on the Singular Value Decomposition (SVD) of the response matrix. We begin in section 4.1 with the SVD analysis in the noiseless case. This uses the rank calculation of the matrix of Green's functions given in section 4.2. The effect of the additive noise on the SVD is discussed in section 4.3.

4.1. SVD analysis of the noiseless data matrix. Let us introduce the $3N \times 3$ matrix $\mathcal{G}(\vec{y})$ of Green's functions, with block structure

$$\mathcal{G}(\vec{y}) = \begin{pmatrix} \mathbf{G}(\vec{x}_1, \vec{y}) \\ \vdots \\ \mathbf{G}(\vec{x}_N, \vec{y}) \end{pmatrix}, \quad (4.1)$$

and use the reciprocity relation $\mathbf{G}(\vec{x}, \vec{y}) = \mathbf{G}(\vec{y}, \vec{x})^T$ to write the model in (3.8) as

$$\mathbf{D} = \sum_{p=1}^P \mathcal{G}(\vec{y}_p) \rho_p \mathcal{G}(\vec{y}_p)^T. \quad (4.2)$$

We show in section 4.2 that in our setting $\mathcal{G}(\vec{y})$ is full rank, so let

$$\mathcal{G}(\vec{y}) = \mathbf{H}(\vec{y}) \mathbf{\Sigma}(\vec{y}) \mathbf{V}(\vec{y})^\dagger \quad (4.3)$$

be its SVD, with $\mathbf{H} \in \mathbb{C}^{3N \times 3}$ satisfying $\mathbf{H}^\dagger \mathbf{H} = \mathbf{I}_3$, and unitary $\mathbf{V} \in \mathbb{C}^{3 \times 3}$. The singular values of $\mathcal{G}(\vec{y})$ are in the diagonal positive definite 3×3 matrix $\mathbf{\Sigma}(\vec{y})$. Substituting (4.3) in (4.2) gives

$$\mathbf{D} = \sum_{p=1}^P \mathbf{H}(\vec{y}_p) \mathcal{R}_p \mathbf{H}(\vec{y}_p)^T, \quad (4.4)$$

with complex symmetric 3×3 matrices

$$\mathcal{R}_p = \mathbf{\Sigma}(\vec{y}_p) \mathbf{V}(\vec{y}_p)^\dagger \rho_p \overline{\mathbf{V}(\vec{y}_p)} \mathbf{\Sigma}(\vec{y}_p), \quad (4.5)$$

where the bar denotes complex conjugate. Moreover, if

$$\mathcal{R}_p = \mathbf{U}_p \mathbf{\mathfrak{S}}_p \mathbf{V}_p^\dagger \quad (4.6)$$

is an SVD of \mathcal{R}_p , we obtain from (4.4) that

$$\mathbf{D} = \sum_{p=1}^P \mathbf{H}(\vec{y}_p) \mathbf{U}_p \mathbf{\mathfrak{S}}_p \mathbf{V}_p^\dagger \mathbf{H}(\vec{y}_p)^T. \quad (4.7)$$

Our imaging algorithm uses the relation between the column space (range) of $\mathcal{G}(\vec{y})$, or equivalently $\mathbf{H}(\vec{y})$, and the subspace spanned by the left singular vectors of \mathbf{D} . This follows from (4.7) and depends on the number of inclusions and their separation distance, as we now explain.

Single inclusion. When $P = 1$ we see from (4.7) that \mathbf{D} has an SVD with nonzero singular values $\sigma_1, \sigma_2, \sigma_3$, the entries in $\mathbf{\mathfrak{S}}_1$, and a $3N \times 3$ matrix of corresponding left singular vectors $\mathbf{H}(\vec{y}_1) \mathbf{U}_1$. However, even when the singular values are distinct, the singular vectors are defined up to an arbitrary phase, so we cannot assume that the

computed $3N \times 3$ matrix \mathbf{U} of left singular vectors of \mathbf{D} equals $\mathbf{H}(\vec{\mathbf{y}}_1)\mathbf{U}_1$. We work instead with projection matrices which are uniquely defined, and satisfy

$$\mathbf{U}\mathbf{U}^\dagger = \mathbf{H}(\vec{\mathbf{y}}_1)\mathbf{U}_1\mathbf{U}_1^\dagger\mathbf{H}(\vec{\mathbf{y}}_1)^\dagger = \mathbf{H}(\vec{\mathbf{y}}_1)\mathbf{H}(\vec{\mathbf{y}}_1)^\dagger, \quad (4.8)$$

because \mathbf{U}_1 is unitary. We conclude that the column space of \mathbf{D} is the same as that of $\mathcal{G}(\vec{\mathbf{y}}_1)$, and moreover, that the $3N \times 3N$ projection on this space can be calculated as $\mathbf{U}\mathbf{U}^\dagger$ using the left singular vectors of \mathbf{D} , or equivalently as $\mathbf{H}(\vec{\mathbf{y}}_1)\mathbf{H}(\vec{\mathbf{y}}_1)^\dagger$, using the left singular vectors of $\mathcal{G}(\vec{\mathbf{y}}_1)$.

Multiple inclusions. When $1 < P < N$, the rank of \mathbf{D} depends on the locations of the inclusions [15]. Generically* it equals $3P$, as we assume here to simplify the presentation. Let $\sigma_1, \dots, \sigma_{3P}$ be the nonzero singular values of \mathbf{D} and

$$\mathbf{U} = (\mathbf{u}_1, \dots, \mathbf{u}_{3P})$$

the $3N \times 3P$ matrix of its corresponding left singular vectors. The projections $\mathbf{H}(\vec{\mathbf{y}}_p)\mathbf{H}(\vec{\mathbf{y}}_p)^\dagger$ are no longer the same as those obtained from $3N \times 3$ blocks in \mathbf{U} , unless the inclusions are so far apart that the column spaces of $\mathcal{G}(\vec{\mathbf{y}}_p)$ and $\mathcal{G}(\vec{\mathbf{y}}_{p'})$ are orthogonal for $p \neq p'$. Nearby inclusions interact and the singular values and vectors of \mathbf{D} are not associated with a single inclusion. However, we conclude from (4.2) and (4.7) that

$$\text{range}(\mathcal{G}(\vec{\mathbf{y}}_p)) = \text{range}(\mathbf{H}(\vec{\mathbf{y}}_p)) \subset \text{range}(\mathbf{D}) = \text{span}\{\mathbf{u}_1, \dots, \mathbf{u}_{3P}\}. \quad (4.9)$$

Moreover, it is shown in [5, Proposition 4.3] that

$$\mathcal{G}(\vec{\mathbf{y}})\vec{\mathbf{e}} \in \text{range}(\mathbf{D}) \quad \text{iff} \quad \vec{\mathbf{y}} \in \{\vec{\mathbf{y}}_1, \dots, \vec{\mathbf{y}}_P\}, \quad (4.10)$$

for any $\vec{\mathbf{e}}$ such that $\mathcal{G}(\vec{\mathbf{y}})\vec{\mathbf{e}} \neq 0$. In our setting $\mathcal{G}(\vec{\mathbf{y}})$ has full rank, so (4.10) holds for any unit vector $\vec{\mathbf{e}} \in \mathbb{R}^3$. This implies in particular that the left singular vectors of $\mathcal{G}(\vec{\mathbf{y}})$, the columns of $\mathbf{H}(\vec{\mathbf{y}})$, are in the range of \mathbf{D} if and only if $\vec{\mathbf{y}}$ coincides with the location of an inclusion.

The results are very similar for incomplete measurements, with data modeled by

$$\mathbf{D}_s = \sum_{p=1}^P \mathcal{G}_s(\vec{\mathbf{y}}_p) \rho_p \mathcal{G}_s(\vec{\mathbf{y}}_p)^T, \quad (4.11)$$

in terms of the $|\mathcal{S}|N \times 3$ matrices of Green's functions

$$\mathcal{G}_s(\vec{\mathbf{y}}) = \text{diag}(\mathbf{S}^T, \dots, \mathbf{S}^T) \mathcal{G}(\vec{\mathbf{y}}). \quad (4.12)$$

We show in the next section that the rank of \mathcal{G}_s is still three, as in the complete measurement case, but its condition number may be much worse. This plays a role in the inversion with noisy measurements. We denote with the same symbol \mathbf{U} the matrix of left singular vectors of \mathbf{D}_s and $\mathbf{H}(\vec{\mathbf{y}})$ the matrix of left singular vectors of $\mathcal{G}_s(\vec{\mathbf{y}})$. We conclude as in the complete measurement case that when $P = 1$,

$$\mathbf{U}\mathbf{U}^\dagger = \mathbf{H}(\vec{\mathbf{y}}_1)\mathbf{H}(\vec{\mathbf{y}}_1)^\dagger,$$

and when $1 < P < N$, using [5, Proposition 4.3],

$$\text{range}(\mathcal{G}_s(\vec{\mathbf{y}})) = \text{range}(\mathbf{H}(\vec{\mathbf{y}})) \subset \text{range}(\mathbf{D}_s) \quad \text{iff} \quad \vec{\mathbf{y}} \in \{\vec{\mathbf{y}}_1, \dots, \vec{\mathbf{y}}_P\}. \quad (4.13)$$

*The rank may be smaller than $3P$ for very special locations of the inclusions [15].

4.2. Rank and conditioning of matrix of Green's functions. As mentioned above and explained in section 5, the rank and condition number of $\mathcal{G}(\vec{y})$ play a role in imaging with noisy measurements. We analyze them here using the Hermitian matrix

$$\begin{aligned}\mathcal{Q}(\vec{y}) &= \mathcal{G}(\vec{y})^\dagger \mathcal{G}(\vec{y}) = \sum_{r=1}^N \mathbf{G}(\vec{x}_r, \vec{y})^\dagger \mathbf{G}(\vec{x}_r, \vec{y}) \\ &\approx \sum_{r=1}^N \frac{1}{(4\pi|\vec{x}_r - \vec{y}|)^2} \left[\mathbf{I}_3 - \frac{(\vec{x}_r - \vec{y})(\vec{x}_r - \vec{y})^T}{|\vec{x}_r - \vec{y}|^2} \right],\end{aligned}\quad (4.14)$$

whose eigenvalues equal the square of the singular values of $\mathcal{G}(\vec{y})$, the entries in $\Sigma(\vec{y})$. The approximation in (4.14) uses definition (2.6) of the Green's tensor, written as

$$\mathbf{G}(\vec{x}_r, \vec{y}) = \frac{e^{ik|\vec{x}_r - \vec{y}|}}{4\pi|\vec{x}_r - \vec{y}|} \left[\mathbf{I}_3 - \frac{(\vec{x}_r - \vec{y})(\vec{x}_r - \vec{y})^T}{|\vec{x}_r - \vec{y}|^2} \right] + O\left(\frac{1}{kL}\right), \quad (4.15)$$

and neglects the $O(1/(kL))$ residual which is small when the inclusions are many wavelengths away from the array.

Equation (4.14) shows that $\mathcal{Q}(\vec{y})$ is, up to some scalar factors, the sum of projection matrices on the plane orthogonal to $\vec{x}_r - \vec{y}$. As \vec{x}_r varies in the array aperture, $\vec{x}_r - \vec{y}$ changes direction in a cone of opening angle of order a/L . The smaller this angle, the worse the conditioning of $\mathcal{Q}(\vec{y})$. Then let us consider the small aperture regime $a \ll L$, where we can approximate the right hand side in (4.14) by

$$\mathcal{Q}(\vec{y}) \approx \frac{N}{(4\pi L)^2} \left[\mathbf{I}_3 - \vec{e}_3 \vec{e}_3^T - \frac{a}{LN} \sum_{r=1}^N \begin{pmatrix} \frac{az_{r,1}^2}{L} & \frac{az_{r,1}z_{r,2}}{L} & -z_{r,1} \\ \frac{az_{r,1}z_{r,2}}{L} & \frac{az_{r,2}^2}{L} & -z_{r,2} \\ -z_{r,1} & -z_{r,2} & -\frac{a|z_r|^2}{L} \end{pmatrix} \right], \quad (4.16)$$

using the notation

$$\mathbf{z}_r = (\mathbf{x}_r - \mathbf{y})/a = (z_{r,1}, z_{r,2}),$$

for $\vec{x}_r = (\mathbf{x}_r, 0)$ and $\vec{y} = (\mathbf{y}, L)$ satisfying $|\mathbf{y}| \lesssim a \ll L$. Here we neglected an $O(a^3/L^3)$ matrix residual in the sum over the N sensors. The leading part of (4.16), $N/(4\pi L)^2 [\mathbf{I}_3 - \vec{e}_3 \vec{e}_3^T]$, is proportional to the orthogonal projection on the cross-range plane, and determines the two larger eigenvalues of $\mathcal{Q}(\vec{y})$, which are approximately $N/(4\pi L)^2$. The third eigenvalue is much smaller, by a factor of order a^2/L^2 . Thus, $\mathcal{Q}(\vec{y})$ is full rank, but it is poorly conditioned in the small aperture regime.

For incomplete measurements we can determine the rank of $\mathcal{G}_s(\vec{y})$ from that of

$$\mathcal{Q}_s(\vec{y}) = \mathcal{G}_s(\vec{y})^\dagger \mathcal{G}_s(\vec{y}) = \sum_{r=1}^N \mathbf{G}(\vec{x}_r, \vec{y})^\dagger \mathbf{S} \mathbf{S}^T \mathbf{G}(\vec{x}_r, \vec{y}). \quad (4.17)$$

The estimation of the eigenvalues of $\mathcal{Q}_s(\vec{y})$ is similar to the above. We obtain that when $a \ll L$, and for measurements along a single direction \vec{e}_1 or \vec{e}_2 , the matrix $\mathcal{Q}(\vec{y})$ has one large eigenvalue approximated by $N/(4\pi L)^2$, a second eigenvalue smaller by a factor of order a^2/L^2 , and an even smaller third one. When the measurements are made in the longitudinal direction \vec{e}_3 , all the eigenvalues are much smaller than $N/(4\pi L)^2$. This is the worse measurement setup. Finally, when all the transversal components of the field are measured, we note that since

$$\mathbf{S} \mathbf{S}^T = \mathbf{I}_3 - \vec{e}_3 \vec{e}_3^T, \quad \mathbf{S} = (\vec{e}_1, \vec{e}_2),$$

\mathcal{Q}_s is a small perturbation of \mathcal{Q} . It has almost the same condition number as $\mathcal{Q}(\vec{y})$, and this improves as the ratio a/L grows.

4.3. Additive noise effects on the SVD. To unify the discussion for complete and incomplete measurements, let us consider the generic problem

$$\tilde{\mathbf{B}} = \mathbf{B} + \mathbf{W}, \quad (4.18)$$

for a low rank \mathfrak{R} matrix $\mathbf{B} \in \mathbb{C}^{M \times M}$ corrupted with additive noise. In our context $M = 3N$ for complete measurements and $|\mathcal{S}|N$ for incomplete ones, and $\mathfrak{R} = 3P$. Moreover, $\tilde{\mathbf{B}}$ equals $\tilde{\mathbf{D}}$ or $\tilde{\mathbf{D}}_s$, and it is modeled by (3.11) and (3.14) in the Hadamard data acquisition scheme described in section 3.2. The noise matrix \mathbf{W} has mean zero and independent, identically distributed complex Gaussian entries of standard deviation σ/\sqrt{M} .

The matrix $\tilde{\mathbf{B}}$ has singular values $\tilde{\sigma}_j$ and left singular vectors $\tilde{\mathbf{u}}_j$, for $j = 1, \dots, M$. Its rank is typically M because of the almost surely full rank noise matrix, but we are interested in its few singular values that can be distinguished from noise, and the associated singular vectors. These are perturbations of the singular values σ_j and left singular vectors \mathbf{u}_j of \mathbf{B} , for $j = 1, \dots, \mathfrak{R}$, and are described below in the asymptotic limit $M \rightarrow \infty$.

We begin with the asymptotic approximation of the square of the Frobenius norm

$$\|\tilde{\mathbf{B}}\|_F^2 = \sum_{j,q=1}^M |\tilde{B}_{jq}|^2 = \sum_{j=1}^M \tilde{\sigma}_j^2,$$

which satisfies [21, 19, 8, 13].

$$M \left(\frac{1}{M} \sum_{j=1}^M \tilde{\sigma}_j^2 - \sigma^2 \right) \rightarrow \sum_{j=1}^{\mathfrak{R}} \sigma_j^2 + \sigma^2 \mathcal{Z}_0, \quad \text{as } M \rightarrow \infty, \quad (4.19)$$

where the convergence is in distribution, and \mathcal{Z}_0 follows a Gaussian distribution with mean zero and variance one. We use this result in section 5 to estimate the noise level σ from the measurements. The behavior of the leading singular values and singular vectors of $\tilde{\mathbf{B}}$ described in the next theorem is used in section 5 to obtain a robust localization of the inclusions.

THEOREM 4.1. *Let $\mathbf{B} \in \mathbb{C}^{M \times M}$ be the matrix of fixed rank \mathfrak{R} in (4.18), and $\tilde{\mathbf{B}}$ its corrupted version by the noise matrix \mathbf{W} with mean zero, independent, identically distributed complex Gaussian entries of standard deviation σ/\sqrt{M} .*

(i) *For $j = 1, \dots, \mathfrak{R}$, and in the limit $M \rightarrow \infty$, the perturbed singular values satisfy*

$$\sqrt{M} \left[\tilde{\sigma}_j - \sigma_j \left(1 + \frac{\sigma^2}{\sigma_j^2} \right) \right] \rightarrow \frac{\sigma}{\sqrt{2}} \left(1 - \frac{\sigma^2}{\sigma_j^2} \right)^{1/2} \mathcal{Z}_0, \quad \text{if } \sigma_j > \sigma, \quad (4.20)$$

and

$$M^{2/3}(\tilde{\sigma}_j - 2\sigma) \rightarrow \frac{\sigma}{2^{2/3}} \mathcal{Z}_2, \quad \text{if } \sigma_j < \sigma, \quad (4.21)$$

where the convergence is in distribution, \mathcal{Z}_0 follows a Gaussian distribution with mean zero and variance one, and \mathcal{Z}_2 follows a type-2 Tracy Widom distribution.

(ii) *Under the additional assumption that the \mathfrak{R} nonzero singular values of \mathbf{B} are*

distinct, and for indices j such that $\sigma_j > \sigma$, the left singular vectors \mathbf{u}_j and $\tilde{\mathbf{u}}_j$ of \mathbf{B} and $\tilde{\mathbf{B}}$ satisfy in the limit $M \rightarrow \infty$

$$|\tilde{\mathbf{u}}_j^\dagger \mathbf{u}_j|^2 \rightarrow 1 - \frac{\sigma^2}{\sigma_j^2}, \quad (4.22)$$

and for $q \neq j \leq \mathfrak{R}$,

$$|\tilde{\mathbf{u}}_q^\dagger \mathbf{u}_j| \rightarrow 0, \quad (4.23)$$

where the convergence is in probability.

The type-2 Tracy-Widom distribution has the cumulative distribution function Φ_{TW2} given by

$$\Phi_{\text{TW2}}(z) = \exp\left(-\int_z^\infty (x-z)\varphi^2(x)dx\right), \quad (4.24)$$

with $\varphi(x)$ the solution of the Painlevé equation

$$\varphi''(x) = x\varphi(x) + 2\varphi(x)^3, \quad \varphi(x) \simeq \text{Ai}(x), \quad x \rightarrow \infty, \quad (4.25)$$

and Ai the Airy function. The expectation of \mathcal{Z}_2 is $\mathbb{E}[\mathcal{Z}_2] \simeq -1.771$ and its variance is $\text{Var}(\mathcal{Z}_2) \simeq 0.813$. Details about the Tracy-Widom distributions can be found in [9].

Theorem 4.1 was already stated in [17] for the special case $\mathfrak{R} = 1$. The proof of the extension to an arbitrary rank \mathfrak{R} can be obtained from the method described in [10]. Note that formula (4.20) seems to predict that the standard deviation of the perturbed singular value $\tilde{\sigma}_j$ cancels when $\sigma_j \searrow \sigma$, but this is true only to leading order $M^{-1/2}$. In fact the standard deviation becomes of order $M^{-2/3}$. Following [8], we can anticipate that there are interpolating distributions which appear when $\sigma_j = \sigma + wM^{-1/3}$ for some fixed w .

5. Inversion with noisy data. We use the singular value decomposition analysis in the previous section to obtain a robust inversion method for noisy array data. We begin in section 5.1 with the estimation of the noise level. Then we formulate in section 5.2 the method for localizing the inclusions. The estimation of their reflectivity tensor is described in section 5.3.

5.1. Estimation of the noise level. A detailed analysis of the estimation of σ , for a variety of cases, is given in [17]. Here $N \gg P$ and we assume that at least one singular value of the noisy data matrix can be distinguished from the others, so we can image. This simplifies the estimation of σ , as we now explain.

Let us begin by rewriting (4.19) as

$$\sum_{j=\mathfrak{R}+1}^M \tilde{\sigma}_j^2 - (M - 4\mathfrak{R})\sigma^2 \sim \sum_{j=1}^{\mathfrak{R}} [\sigma_j^2 - (\tilde{\sigma}_j^2 - 4\sigma^2)] + \sigma^2 \mathcal{Z}_0, \quad (5.1)$$

where we recall that $\mathfrak{R} = 3P$, and $M = 3N$ for complete measurements and $|\mathcal{S}|N$ otherwise. The symbol \sim stands for approximate, in the asymptotic regime $M \gg 1$, and there is no bias in the right hand side in the absence of the inclusions i.e., when $\sigma_j = 0$ and $\tilde{\sigma}_j \sim 2\sigma$ for the first indices j by (4.21).

The unbiased estimate of the noise level σ follows from (5.1),

$$\sigma^e = \frac{1}{M - 4\mathfrak{R}} \sum_{j=\mathfrak{R}+1}^M \tilde{\sigma}_j^2, \quad (5.2)$$

but it requires prior knowledge of the number of inclusions. If this is unknown, we can use the empirical estimate

$$\sigma^e = \frac{1}{M - 4\mathfrak{R}^e} \sum_{j=\mathfrak{R}^e+1}^M \tilde{\sigma}_j^2, \quad (5.3)$$

where \mathfrak{R}^e is the number of singular values of $\tilde{\mathbf{B}}$ that are significantly larger than the others. The estimate (5.3) is very close to (5.2) because $M \gg \mathfrak{R} \geq \mathfrak{R}^e$.

5.2. Localization of the inclusions. We assume henceforth that the noiseless matrix \mathbf{B} , equal to \mathbf{D} for complete measurements and \mathbf{D}_s for incomplete ones, has $\mathfrak{R} = 3P$ distinct singular values indexed in decreasing order as $\sigma_1, \dots, \sigma_{\mathfrak{R}}$. The corresponding left singular vectors are the columns \mathbf{u}_j of the $M \times \mathfrak{R}$ matrix

$$\mathbf{U} = (\mathbf{u}_1, \dots, \mathbf{u}_{\mathfrak{R}}). \quad (5.4)$$

The singular values of the noisy matrix $\tilde{\mathbf{B}}$ are denoted by $\tilde{\sigma}_j$, for $j = 1, \dots, M$. We are interested in the first $\tilde{\mathfrak{R}}$ of them, which can be distinguished from the noise.

The effective rank $\tilde{\mathfrak{R}}$ is determined using Theorem 4.1,

$$\tilde{\mathfrak{R}} = \max\{j = 1, \dots, M \text{ such that } \tilde{\sigma}_j > \sigma^e r_\theta\}. \quad (5.5)$$

where the threshold r_θ is defined

$$r_\theta = 2 + \frac{1}{(2M)^{\frac{2}{3}}} \Phi_{\text{TW2}}^{-1}(1 - \theta), \quad (5.6)$$

with Φ_{TW2} the cumulative distribution function (4.24) of the Tracy-Widom distribution of type 2. As shown in [17, 2], by the Neyman-Pearson lemma, the decision rule (5.5) maximizes the probability of detection for a given false alarm rate θ . This is a user defined number satisfying $0 < \theta \ll 1$. In our case M is large, so for all θ we collect the singular values that are significantly larger than $2\sigma^e$.

We let

$$\tilde{\mathbf{U}} = (\tilde{\mathbf{u}}_1, \dots, \tilde{\mathbf{u}}_{\tilde{\mathfrak{R}}}) \quad (5.7)$$

be the matrix of the leading left singular vectors of $\tilde{\mathbf{B}}$. The MUSIC method [5] determines the locations of the inclusions by projecting $\mathcal{G}(\vec{\mathbf{y}})\vec{\mathbf{e}}$ or $\mathcal{G}_s(\vec{\mathbf{y}})\vec{\mathbf{e}}$ on the range of $\tilde{\mathbf{U}}$, for some vector $\vec{\mathbf{e}}$ and search points $\vec{\mathbf{y}}$. With $\vec{\mathbf{e}} = \vec{\mathbf{e}}_1$ we obtain the MUSIC imaging function

$$\mathcal{I}_{\text{MUSIC}}(\vec{\mathbf{y}}) = \left\| \left(\mathbf{I}_M - \tilde{\mathbf{U}}\tilde{\mathbf{U}}^\dagger \right) \mathcal{G}(\vec{\mathbf{y}})\vec{\mathbf{e}}_1 \right\|_F^{-1}, \quad (5.8)$$

in the case of complete measurements, where $M = 3N$. It is the same for incomplete measurements, except that $\mathcal{G}(\vec{\mathbf{y}})$ is replaced by $\mathcal{G}_s(\vec{\mathbf{y}})$ and $M = |\mathcal{S}|N$.

If noise were negligible, (5.8) would peak at the locations of the inclusions due to (4.10). As the noise level grows the effective rank $\tilde{\mathfrak{R}}$ decreases, the subspace spanned by the columns of $\tilde{\mathbf{U}}$ changes, and the MUSIC images deteriorate. We show next how to improve the localization method using the results in Theorem 4.1.

5.2.1. Localization of one inclusion or well separated inclusions. The robust localization is based on (4.8) and its equivalent for incomplete measurements, and Theorem 4.1. It consists of the following steps:

Step 1. Estimate the $\tilde{\mathfrak{R}}$ singular values of the unknown unperturbed matrix \mathbf{B} from equation (4.20), rewritten as

$$\tilde{\sigma}_j \approx \sigma_j \left(1 + \frac{\sigma^2}{\sigma_j^2} \right).$$

Replacing σ by its estimate σ^e , and choosing the root that is larger than σ^e , we obtain

$$\sigma_j^e = \frac{1}{2} \left[\tilde{\sigma}_j + \sqrt{\tilde{\sigma}_j^2 - (2\sigma^e)^2} \right], \quad j = 1, \dots, \tilde{\mathfrak{R}}. \quad (5.9)$$

Step 2. Estimate the changes of direction of the leading singular vectors, using (4.22),

$$|\tilde{\mathbf{u}}_j^\dagger \mathbf{u}_j|^2 \approx \cos^2 \theta_j^e = 1 - \left(\frac{\sigma^e}{\sigma_j^e} \right)^2, \quad j = 1, \dots, \tilde{\mathfrak{R}}. \quad (5.10)$$

We also have from (4.23) that

$$|\tilde{\mathbf{u}}_q^\dagger \mathbf{u}_j|^2 \approx 0, \quad j, q = 1, \dots, \tilde{\mathfrak{R}}, \quad j \neq q. \quad (5.11)$$

Step 3. For the search point $\vec{\mathbf{y}}$ calculate the matrix $\mathcal{G}(\vec{\mathbf{y}})$ given by (4.1) for complete measurements, or $\mathcal{G}_s(\vec{\mathbf{y}})$ given by (4.12) for incomplete measurements. Determine the matrix $\mathbf{H}(\vec{\mathbf{y}})$ of their left singular vectors, and calculate

$$\mathbf{T}(\vec{\mathbf{y}}) = \tilde{\mathbf{U}}^\dagger \mathbf{H}(\vec{\mathbf{y}}) \mathbf{H}(\vec{\mathbf{y}})^\dagger \tilde{\mathbf{U}}. \quad (5.12)$$

When $\vec{\mathbf{y}} = \vec{\mathbf{y}}_1$, we conclude from (4.8) that

$$\mathbf{T}(\vec{\mathbf{y}}_1) = \tilde{\mathbf{U}}^\dagger \mathbf{U} \mathbf{U}^\dagger \tilde{\mathbf{U}}.$$

Here \mathbf{U} is unknown, but (5.10)–(5.11) give that the components of $\mathbf{T}(\vec{\mathbf{y}}_1)$ satisfy

$$T_{jq}(\vec{\mathbf{y}}_1) \approx \delta_{jq} \cos^2 \theta_j^e, \quad j, q = 1, \dots, \tilde{\mathfrak{R}}. \quad (5.13)$$

Step 4. Calculate the imaging function

$$\mathcal{I}(\vec{\mathbf{y}}) = \left\{ \sum_{j,q=1}^{\tilde{\mathfrak{R}}} \gamma_j^2 [T_{jq}(\vec{\mathbf{y}}) - \delta_{jq} \cos^2 \theta_j^e]^2 \right\}^{-1/2}, \quad (5.14)$$

where γ_j are some positive weighting coefficients. We use them to emphasize the contributions of the terms for large singular values, and give less weight to those for singular values close to the estimated noise level σ^e . In the numerical simulations

$$\gamma_j = \min \left\{ 1, \frac{3(\sigma_j^e - \sigma^e)}{\sigma^e} \right\}. \quad (5.15)$$

The estimator of $\vec{\mathbf{y}}_1$ is the argument of the maximum of $\mathcal{I}(\vec{\mathbf{y}})$.

This algorithm may be used for localizing multiple inclusions that are sufficiently far apart, so that the column spaces of $\mathbf{H}(\vec{\mathbf{y}}_j)$ and $\mathbf{H}(\vec{\mathbf{y}}_q)$, for $j \neq q$, are approximately orthogonal. To understand what sufficiently far means, we can analyze the decay of the inner products of the columns of $\mathcal{G}(\vec{\mathbf{y}}_j)$ and $\mathcal{G}(\vec{\mathbf{y}}_q)$ with the distance $|\vec{\mathbf{y}}_q - \vec{\mathbf{y}}_j|$. This is similar to studying the spatial support of

$$\mathcal{F}(\vec{\mathbf{y}}_j, \vec{\mathbf{y}}_q) = \sum_{r=1}^N \frac{e^{ik(|\vec{\mathbf{x}}_r - \vec{\mathbf{y}}_q| - |\vec{\mathbf{x}}_r - \vec{\mathbf{y}}_j|)}}{(4\pi)^2 |\vec{\mathbf{x}}_r - \vec{\mathbf{y}}_j| |\vec{\mathbf{x}}_r - \vec{\mathbf{y}}_q|}, \quad (5.16)$$

the point spread function of the reverse time (Kirchhoff) migration method for sonar imaging. The known resolution limits of this method give that the inclusions are well separated when

$$|\mathbf{y}_q - \mathbf{y}_j| \gg \frac{\lambda L}{a}, \quad |y_{q,3} - y_{j,3}| \gg \frac{\lambda L^2}{a^2}. \quad (5.17)$$

Here we used the notation $\vec{\mathbf{y}}_q = (\mathbf{y}_q, y_{q,3})$ and similar for $\vec{\mathbf{y}}_j$.

5.2.2. Localization of multiple inclusions. Imaging of nearby inclusions is more difficult because they interact, and multiple inclusions may be associated with one singular value and vector. To address this case we modify Steps 3-4 of the imaging method using the results (4.9)–(4.10), which imply that

$$\mathbf{h}_q(\vec{\mathbf{y}}) = \sum_{l=1}^{\Re} [\mathbf{u}_l^\dagger \mathbf{h}_q(\vec{\mathbf{y}})] \mathbf{u}_l \quad \text{iff } \vec{\mathbf{y}} \in \{\vec{\mathbf{y}}_1, \dots, \vec{\mathbf{y}}_P\}. \quad (5.18)$$

Here $\mathbf{h}_q(\vec{\mathbf{y}})$ are the left singular vectors of $\mathcal{G}(\vec{\mathbf{y}})$, the columns of $\mathbf{H}(\vec{\mathbf{y}})$ for $q = 1, 2, 3$, and the right hand side is their projection on the span of $\{\mathbf{u}_1, \dots, \mathbf{u}_{\Re}\}$, the range of the noiseless data matrix. It suffices to work with $q = 1$, which gives the largest contribution to the data model in equations (4.4)–(4.5). The analysis in section 4.2 shows that the third singular value of $\mathcal{G}(\vec{\mathbf{y}})$ is very small in the small aperture regime, and for incomplete measurements along $\vec{\mathbf{e}}_1$ or $\vec{\mathbf{e}}_2$ the matrix $\mathcal{G}_s(\vec{\mathbf{y}})$ has only one large singular value. Thus, the terms with \mathbf{h}_2 and \mathbf{h}_3 may give small contributions to \mathbf{D} or \mathbf{D}_s and consequently, \mathbf{h}_2 and \mathbf{h}_3 may have small projections on the subspace spanned by $\{\mathbf{u}_j\}_{1 \leq j \leq \tilde{\Re}}$ when $j \leq \Re < \tilde{\Re}$. This is why we use \mathbf{h}_1 in the localization.

We cannot work with (5.18) directly, because we do not know the unperturbed singular vectors. However, we can calculate their projection on the span $\{\tilde{\mathbf{u}}_l\}$ for $l = 1, \dots, \tilde{\Re}$, which satisfies by (5.11) and (5.18)

$$\tilde{\mathbf{u}}_l [\tilde{\mathbf{u}}_l^\dagger \mathbf{h}_1(\vec{\mathbf{y}})] = \tilde{\mathbf{u}}_l \sum_{q=1}^{\Re} (\tilde{\mathbf{u}}_l^\dagger \mathbf{u}_q) [\mathbf{u}_q^\dagger \mathbf{h}_1(\vec{\mathbf{y}})] \approx \tilde{\mathbf{u}}_l (\tilde{\mathbf{u}}_l^\dagger \mathbf{u}_1) [\mathbf{u}_1^\dagger \mathbf{h}_1(\vec{\mathbf{y}})], \quad (5.19)$$

for $\vec{\mathbf{y}} \in \{\vec{\mathbf{y}}_1, \dots, \vec{\mathbf{y}}_P\}$. Taking the Euclidian norm in (5.19) and using (5.10) we obtain

$$|\mathbf{u}_l^\dagger \mathbf{h}_1(\vec{\mathbf{y}})| \approx \frac{|\tilde{\mathbf{u}}_l^\dagger \mathbf{h}_1(\vec{\mathbf{y}})|}{|\cos \theta_l|}, \quad l = 1, \dots, \tilde{\Re}, \quad (5.20)$$

and the norm of (5.18) gives

$$1 = \|\mathbf{h}_1(\vec{\mathbf{y}})\|^2 = \sum_{l=1}^{\Re} |\mathbf{u}_l^\dagger \mathbf{h}_1(\vec{\mathbf{y}})|^2, \quad \vec{\mathbf{y}} \in \{\vec{\mathbf{y}}_1, \dots, \vec{\mathbf{y}}_P\}. \quad (5.21)$$

We have only the first $\tilde{\mathfrak{R}}$ terms in the right hand side of (5.21), and we use them to obtain the imaging function

$$\mathcal{I}(\vec{y}) = \left[1 - \sum_{j=1}^{\tilde{\mathfrak{R}}} \frac{|\tilde{\mathbf{u}}_j^\dagger \mathbf{h}_1(\vec{y})|^2}{\cos^2 \theta_j^e} \right]^{-1/2} \quad (5.22)$$

We expect from (5.18) that when $\tilde{\mathfrak{R}} = \mathfrak{R}$, the imaging function (5.22) peaks at $\vec{y} = \vec{y}_j$, for $j = 1, \dots, P$. This happens only for weak noise. In general $\tilde{\mathfrak{R}} < \mathfrak{R}$, and (5.22) peaks at the location of the stronger inclusions, which contribute to the $\tilde{\mathfrak{R}}$ distinguishable singular values.

5.3. Estimation of the reflectivity tensor. If we knew the locations $\{\vec{y}_p\}_{1 \leq p \leq P}$ of the inclusions, we could obtain from (3.11) and (4.4) that

$$\mathbf{H}(\vec{y}_p)^\dagger \tilde{\mathbf{D}} \overline{\mathbf{H}(\vec{y}_p)} = \mathcal{R}_p + \Delta \mathcal{R}_p, \quad p = 1, \dots, P. \quad (5.23)$$

This is for complete measurements, and the error

$$\Delta \mathcal{R}_p = \mathbf{H}(\vec{y}_p)^\dagger \mathbf{W} \overline{\mathbf{H}(\vec{y}_p)} + \sum_{l \neq p, l=1}^P [\mathbf{H}(\vec{y}_p)^\dagger \mathbf{H}(\vec{y}_l)] \mathcal{R}_l [\mathbf{H}(\vec{y}_p)^\dagger \mathbf{H}(\vec{y}_l)]^T \quad (5.24)$$

is due to the noise and interaction of the inclusions. The interaction is small when the inclusions are well separated.

We only have estimates \vec{y}_p^e of \vec{y}_p , the peaks of the imaging function defined in the previous section, so we calculate instead

$$\tilde{\mathcal{R}}_p = \mathbf{H}(\vec{y}_p^e)^\dagger \tilde{\mathbf{D}} \overline{\mathbf{H}(\vec{y}_p^e)}, \quad p = 1, \dots, P. \quad (5.25)$$

These are modeled by

$$\tilde{\mathcal{R}}_p = \mathcal{R}_p + \tilde{\Delta} \mathcal{R}_p, \quad (5.26)$$

where $\tilde{\Delta} \mathcal{R}_p$ includes (5.24) and additional terms due to location errors $\vec{y}_p^e - \vec{y}_p$. The estimate of \mathcal{R}_p is motivated by definition (4.5) of \mathcal{R}_p ,

$$\rho_p^e = \Gamma(\vec{y}_p^e) \tilde{\mathcal{R}}_p \Gamma(\vec{y}_p^e)^T, \quad (5.27)$$

where

$$\Gamma(\vec{y}) = \mathbf{V}(\vec{y}) \Sigma(\vec{y})^{-1}. \quad (5.28)$$

Recall from (4.3) that $\Sigma(\vec{y})$ is the 3×3 matrix of singular values of $\mathcal{G}(\vec{y})$ and $\mathbf{V}(\vec{y})$ the 3×3 matrix of its right singular vectors.

We can model (5.27) by

$$\rho_p^e = \rho_p + \Delta \rho_p, \quad (5.29)$$

with error $\Delta \rho_p$ that consists of two parts. The first part depends on the noise, the interaction of the inclusions and the error in their estimated locations

$$\Delta \rho_p^{(1)} = \Gamma(\vec{y}_p^e) \tilde{\Delta} \mathcal{R}_p \Gamma(\vec{y}_p^e)^T. \quad (5.30)$$

The second part vanishes when the inclusion is correctly localized

$$\Delta \rho_p^{(2)} = \Gamma(\vec{y}_p^e) \mathcal{R}_p \Gamma(\vec{y}_p^e)^T - \Gamma(\vec{y}_p) \mathcal{R}_p \Gamma(\vec{y}_p)^T. \quad (5.31)$$

5.3.1. Discussion. The numerical results in section 6 show that the inclusion localization in cross-range is excellent for the case of complete measurements. However, the range localization deteriorates quickly with noise in the small aperture regime. This can be understood from the analysis in section 4.2, equation (4.16) in particular, which shows that $\mathbf{Q}(\vec{\mathbf{y}}) = \mathbf{G}(\vec{\mathbf{y}})^\dagger \mathbf{G}(\vec{\mathbf{y}})$ has two leading orthonormal eigenvectors \mathbf{v}_q which are approximately in $\text{span}\{\vec{\mathbf{e}}_1, \vec{\mathbf{e}}_2\}$, for $q = 1, 2$. They correspond to eigenvalues that are approximately $N/(4\pi L^2)$. The third eigenvector is $\mathbf{v}_3 \approx \vec{\mathbf{e}}_3$, for a much smaller eigenvalue by a factor of the order of a^2/L^2 . These eigenvalues are the squares of the entries in $\Sigma(\vec{\mathbf{y}})$, and the eigenvectors are the columns of $\mathbf{V}(\vec{\mathbf{y}})$.

We also see from (4.1) and (4.15) that the left singular vectors of $\mathbf{G}(\vec{\mathbf{y}})$ are

$$\mathbf{h}_q(\vec{\mathbf{y}}) \approx N^{-1/2} \begin{pmatrix} e^{ik|\vec{\mathbf{x}}_1 - \vec{\mathbf{y}}|} \mathbf{v}_q \\ \vdots \\ e^{ik|\vec{\mathbf{x}}_N - \vec{\mathbf{y}}|} \mathbf{v}_q \end{pmatrix}, \quad q = 1, 2, \quad a \ll L, \quad (5.32)$$

with phases

$$k|\vec{\mathbf{x}}_r - \vec{\mathbf{y}}| = kL \left(1 + \frac{y_3 - L}{L} + \frac{|\mathbf{x}_r - \mathbf{y}|^2}{2L^2} \right) + O\left(\frac{a^3}{\lambda L}\right). \quad (5.33)$$

These vectors define the projection matrices $\mathbf{h}_q(\vec{\mathbf{y}})\mathbf{h}_q(\vec{\mathbf{y}})^\dagger$ used in the localization method, for $q = 1, 2$. The singular vector $\mathbf{h}_3(\vec{\mathbf{y}})$ is unlikely to play a role when noise is present. Moreover, the projection matrices are approximately independent of the range component y_3 of $\vec{\mathbf{y}} = (\mathbf{y}, y_3)$, due to cancellation in the difference of the phase (5.33). Thus, range estimation becomes impossible in the small aperture regime.

Both terms in the error Δ_{ρ_p} in the estimation of the reflectivity tensor (5.27) have large components when the diagonal matrix $\Sigma = \text{diag}(\Sigma_1, \Sigma_2, \Sigma_3)$ has a small entry. This is because we take its inverse in (5.28). Since in the small aperture regime

$$\Sigma_3(\vec{\mathbf{y}}) \ll \Sigma_1(\vec{\mathbf{y}}) \approx \Sigma_2(\vec{\mathbf{y}}),$$

and the third column of $\mathbf{V}(\vec{\mathbf{y}})$ is approximately $\vec{\mathbf{e}}_3$, we expect $(\Delta_{\rho_p})_{ij}$ to be large for i or j equal to 3. The other components of the error should be of the order of the noise and inclusion interaction. This is indeed demonstrated by the numerical simulations in section 6. The condition number of $\Sigma(\vec{\mathbf{y}})$ improves for larger ratios a/L , and so do the estimates of ρ_p .

5.3.2. Incomplete measurements. The estimation of the reflectivity tensors from incomplete measurements can be done formally as above, with $\mathbf{H}(\vec{\mathbf{y}})$ the matrix of left singular vectors of $\mathbf{G}_s(\vec{\mathbf{y}})$ and $\Sigma(\vec{\mathbf{y}})$ the matrix of its singular values. The results are expected to be much worse when only one component of the electric field is measured, that is for $\mathbf{S} = (\vec{\mathbf{e}}_q)$ and some $q \in \{1, 2, 3\}$. As shown in section 4.2, matrix $\Sigma(\vec{\mathbf{y}})$ has at most one large entry in this case, so the effective rank $\tilde{\mathfrak{R}}$ in the presence of noise is smaller than in the complete measurement case. This translates into worse localization of the inclusions. Moreover, more components of the errors Δ_{ρ_p} are large, due to the inversion of $\Sigma(\vec{\mathbf{y}})$ in (5.28).

6. Numerical results. In this section we present numerical results that assess the performance of the imaging method described in section 5. We begin with the setup of the simulations in section 6.1. Then we compare in section 6.2 the asymptotic limits stated in Theorem 4.1 to the empirical statistics of the singular values and vectors obtained with Monte Carlo simulations. The inversion results are in section 6.3 for one inclusion and in section 6.4 for multiple inclusions.

6.1. Description of the numerical simulations. We present results for two scattering regimes. The first is called a *large aperture regime*, because the array aperture is as large as the range of the inclusions $L = a = 10\lambda$. The second is a *small aperture regime* with $L = 100\lambda \gg a = 10\lambda$. The sensors are placed on a regular square grid in the array aperture, with spacing $\lambda/2$, so $N = 441$. The three-dimensional search domain is sampled in steps of $\lambda/2$.

We model the scattered field using equation (3.2), for inclusions with reflectivity tensor (3.3). Since the equation is linear, we factor out the small scaling factor α^3 . The inclusions are ellipsoids with scaled semiaxes $a_{p,j}$, for $p = 1, \dots, P$ and $j = 1, 2, 3$. Their scaled volume is

$$|\Omega_p| = \frac{4\pi}{3} \prod_{q=1}^3 a_{p,q}.$$

In a system of coordinates with axes of the ellipsoid, the polarization tensor in (3.3) is diagonal. We use the system of coordinates centered at the array, with basis $\{\vec{e}_1, \vec{e}_2, \vec{e}_3\}$, which is a rotation of that of the ellipsoids by some matrix \mathcal{R}_p . The polarization tensors are [5]

$$\mathbf{M}_p = |\Omega_p| \mathcal{R}_p \text{diag} \left(\frac{1}{1 + (\epsilon_p/\epsilon_o - 1)\mathcal{D}_{p,q}}, q = 1, 2, 3 \right) \mathcal{R}_p^T, \quad (6.1)$$

where $\mathcal{D}_{p,q}$ are the depolarization factors of the ellipsoids [23, Section 3.3], given by the elliptic integrals

$$\mathcal{D}_{p,q} = \frac{|\Omega_p|}{2} \int_0^\infty \frac{ds}{(s + a_{p,q}^2) [\prod_{l=1}^3 (s + a_{p,l}^2)]^{1/2}}. \quad (6.2)$$

For example, in the case of one inclusion at $\vec{y}_1 = (1, -1, L)$, we take $a_{1,q} = q$, for $q = 1, 2, 3$, the contrast $\epsilon_1/\epsilon_o = 10$, and some rotation \mathcal{R}_1 to obtain the reflectivity tensor

$$\alpha^{-3} \boldsymbol{\rho}_1 = \begin{pmatrix} 55.4 & -7.28 & -13.43 \\ -7.28 & 70.82 & -22.64 \\ -13.43 & -22.64 & 70.75 \end{pmatrix}. \quad (6.3)$$

The noise matrix \mathbf{W} is generated with the MATLAB command *randn*, as in

$$\mathbf{W} = \frac{\sigma}{\sqrt{2M}} (\text{randn}(M) + i \text{randn}(M)), \quad (6.4)$$

where $M = 3N$ for complete measurements and $|\mathcal{S}|N$ for incomplete ones. The noise level σ is chosen as a percentage of the largest singular value σ_1 of the noiseless data matrix \mathbf{D} . Thus, when we say 50% noise, we mean that $\sigma = 0.5\sigma_1$.

Remark: The typical amplitude of the entries of the unperturbed matrix \mathbf{D} is σ_1/M , while the noise entries in \mathbf{W} (with the Hadamard acquisition scheme) have standard deviation σ/\sqrt{M} . Therefore, the measured $\tilde{\mathbf{D}} = \mathbf{D} + \mathbf{W}$ has the signal-to-noise ratio $\text{SNR} = \sigma_1/(\sigma\sqrt{M})$. In the simulations σ/σ_1 varies between 10% and 75%. This is very strong noise. For example, when $\sigma/\sigma_1 = 50\%$, the SNR is $2/\sqrt{M} = 0.05$ in the complete measurement case, where $M = 3N = 1323$. This small SNR means that the signal is very weak and buried in noise.

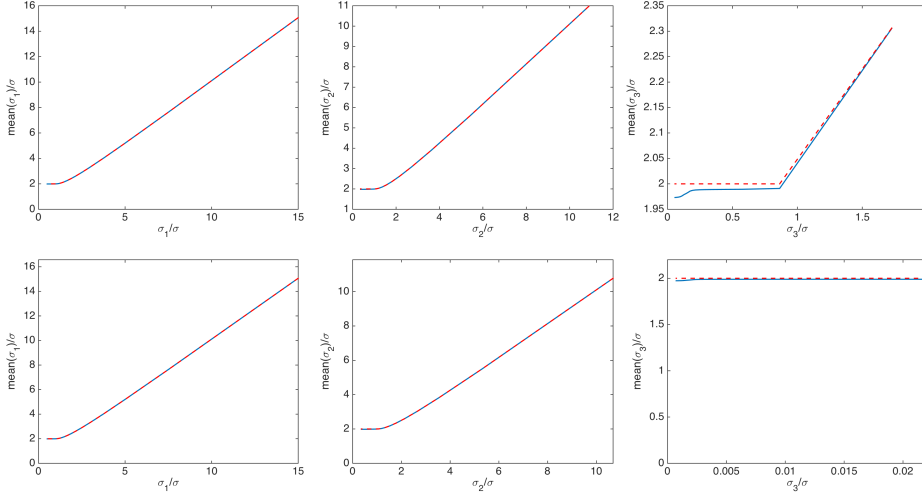


FIG. 6.1. Plots of $\text{mean}[\tilde{\sigma}_j]/\sigma$ vs. σ_j/σ , for $j = 1, 2, 3$. The empirical estimates of the means are shown with solid blue lines and the asymptotic estimates (6.5) are shown with dotted red lines. The top row is for the large aperture regime and the bottom row for the small aperture regime.

6.2. Statistics of the singular values and singular vectors. We compare here the asymptotic behavior of the singular values and singular vectors stated in Theorem 4.1 to the empirical estimates of their statistics obtained with Monte Carlo simulations. We take a single inclusion with reflectivity tensor (6.3) and one thousand samples of the noise matrix (6.4).

6.2.1. Complete measurements. Because there is a single inclusion, the data matrix $\mathbf{B} = \mathbf{D}$ has rank three. In the large aperture regime its singular values are

$$\sigma_1 = 1.703, \quad \sigma_2 = 1.126, \quad \sigma_3 = 0.183,$$

and in the small aperture regime they are

$$\sigma_1 = 0.021, \quad \sigma_2 = 0.015, \quad \sigma_3 = 3.01 \cdot 10^{-5}.$$

The difference in the magnitudes of σ_1 and σ_2 in the two regimes is due to the geometrical spreading factor of order $1/(4\pi L)^2$. As expected from the discussion in section 4.2, we have $\sigma_3 \ll \sigma_2 \lesssim \sigma_1$ in the small aperture regime.

We plot with solid blue lines in Figure 6.1 the empirical means of the singular values $\tilde{\sigma}_j$ of $\tilde{\mathbf{D}}$, for $j = 1, 2, 3$ and $\sigma \in (0, 2\sigma_1)$. The abscissa is σ_j/σ and the ordinate is $\text{mean}[\tilde{\sigma}_j]/\sigma$. The results are in excellent agreement with the asymptotic formulas

$$\tilde{\sigma}_j \approx \begin{cases} \sigma_j (1 + \sigma^2/\sigma_j^2) & \text{if } \sigma_j > \sigma, \\ 2\sigma & \text{if } \sigma_j < \sigma, \end{cases} \quad (6.5)$$

plotted in the figure with dotted red lines. The top row in Figure 6.1 is for the large aperture regime and the bottom row for the small aperture regime. The plots are similar, except that in the small aperture case σ_3 cannot be distinguished from noise.

In Figure 6.2 we plot the standard deviations of $\tilde{\sigma}_j$ and note that they are much smaller than the means, so $\tilde{\sigma}_j$ are approximately deterministic. We show the plots of

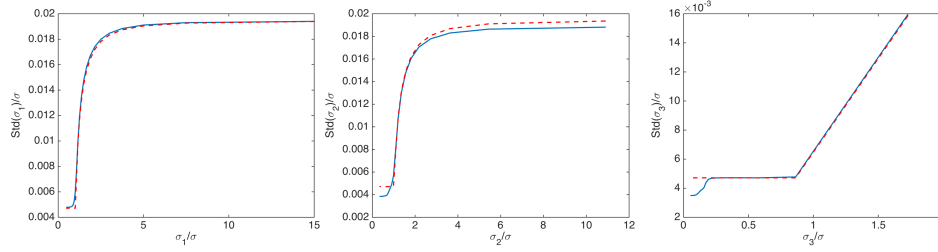


FIG. 6.2. Plots of $\text{std}[\tilde{\sigma}_j]/\sigma$ vs. σ_j/σ , for $j = 1, 2, 3$ in the large aperture regime. The empirical estimates are shown with solid blue lines and the asymptotic estimates (6.6) with dotted red lines.

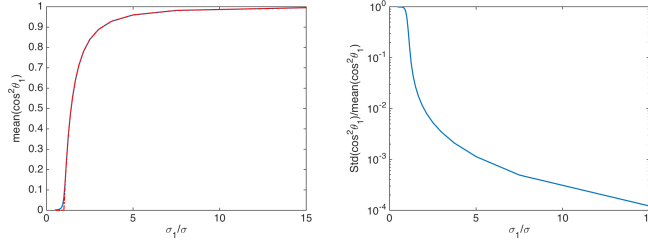


FIG. 6.3. Plots of $\text{mean}[\cos^2 \theta_1]$ (left) and $\text{std}[\cos^2 \theta_1]/\text{mean}[\cos^2 \theta_1]$ (right) vs. σ_1/σ , in the large aperture regime. The empirical estimates are shown with solid blue lines and the asymptotic estimates (6.6) are plotted with dotted red lines.

$\text{std}(\tilde{\sigma}_j)$ in the large aperture regime, and compare them with the asymptotic ones in Theorem 4.1,

$$\text{std}(\tilde{\sigma}_j) \approx \begin{cases} \frac{\sigma}{(6N)^{1/2}} (1 - \sigma^2/\sigma_j^2)^{1/2} & \text{if } \sigma_j > \sigma, \\ \frac{\sigma}{(6N)^{2/3}} \sqrt{0.813} & \text{if } \sigma_j < \sigma. \end{cases} \quad (6.6)$$

Here we used that $\text{std}(\mathcal{Z}_2) \approx \sqrt{0.813}$. The results at small aperture are similar.

In Figure 6.3 we display the empirical mean of $\cos^2 \theta_1 = |\tilde{\mathbf{u}}_1 \mathbf{u}_1|^2$ and compare it with its asymptotic prediction (4.22). We also plot the standard deviation, and note that it is much smaller than the mean when $\sigma_1 > \sigma$, as expected from Theorem 4.1. The plots look the same for the large and small aperture regimes, and for the other angles θ_2 and θ_3 , when σ_2 and σ_3 are greater than σ .

6.2.2. Incomplete measurements. We do not include plots for the incomplete measurements, where $\mathbf{B} = \mathbf{D}_s$, because they do not add much information. Instead, we display below the effect of the sensing matrix \mathbf{S} on the singular values of \mathbf{D}_s . As explained in section 5, we expect that the inversion algorithm will be most effective when the effective rank $\tilde{\mathfrak{R}}$ equals the rank $\mathfrak{R} = 3$ of \mathbf{D}_s . Since $\tilde{\mathfrak{R}}$ is the number of singular values of \mathbf{D}_s that are larger than 2σ , the more small singular values \mathbf{D}_s has, the worse the inversion results.

When $\mathbf{S} = (\tilde{\mathbf{e}}_1)$, the singular values of $\tilde{\mathbf{D}}_s$ are

$$\sigma_1 = 1.099, \quad \sigma_2 = 0.087, \quad \sigma_3 = 0.007$$

in the large aperture regime and

$$\sigma_1 = 0.015, \quad \sigma_2 = 1.7 \cdot 10^{-5}, \quad \sigma_3 = 1.6 \cdot 10^{-8}$$

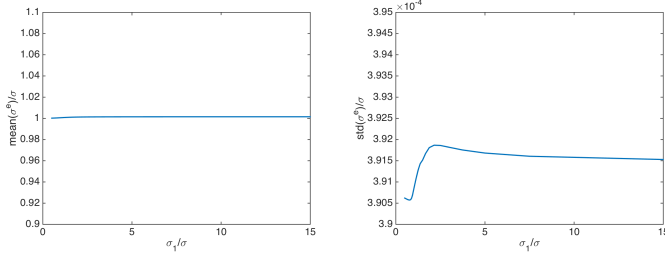


FIG. 6.4. Empirical mean of the noise level estimate (5.2) (left plot) and standard deviation (right plot). The results are normalized by σ . The abscissa is σ_1/σ .

in the small aperture regime. The results are similar for $\mathbf{S} = (\vec{e}_2)$, and show that as predicted by the analysis in section 4.2, only one singular value is large. The case with $\mathbf{S} = (\vec{e}_3)$ is much worse, because all the singular values are small, and are likely to be dominated by noise. Explicitly, we get

$$\sigma_1 = 0.145, \quad \sigma_2 = 0.065, \quad \sigma_3 = 0.023$$

in large aperture regime and

$$\sigma_1 = 2.3 \cdot 10^{-5}, \quad \sigma_2 = 1.3 \cdot 10^{-5}, \quad \sigma_3 = 1.9 \cdot 10^{-7}$$

in the small aperture regime. Finally, when both cross-range components of the electric field are measured using $\mathbf{S} = (\vec{e}_1, \vec{e}_2)$, the singular values of \mathbf{D}_s are similar to those of \mathbf{D} . Thus, we expect inversion results which are comparable to those for complete measurements.

6.2.3. Estimation of the noise level. We display in Figure 6.4 the empirical mean and standard deviation of the unbiased estimate (5.2) of the noise level, using the complete measurement matrix $\tilde{\mathbf{D}}$. We note that $\sigma^e \approx \text{mean}[\sigma^e] \approx \sigma$. The estimate (5.3) is very similar, because we have many sensors. For the same reason we obtain similar estimates of σ from incomplete measurements. If the number of sensors were smaller, then the refined estimation methods proposed in [17] could be used.

6.3. Inversion results for one inclusion. We present results for the inclusion at $\vec{y}_1 = (\lambda, -\lambda, L)$, with reflectivity tensor (6.3), in both the large and small aperture regimes. We compare the MUSIC method (5.8) with the imaging function (5.14), and estimate the reflectivity tensor as in section 5.3.

6.3.1. Complete measurements. Let us begin with Figure 6.5, which shows the surface plots of $\mathcal{I}_{\text{MUSIC}}(\vec{y})$ in the planes $y_3 = L$ and $y_2 = -\lambda$, respectively. These are obtained in the large aperture regime, for two realizations of the noise matrix: one for 25% noise (bottom row) and the other for 75% noise (top row). At the higher noise level the MUSIC function fails to localize the inclusion, as it has no peak. For comparison, we display in Figure 6.6 the results obtained with our imaging function (5.14), for the same realization at 75% noise. We do not show the images for 25% noise because they are similar. The images are a significant improvement over those in Figure 6.5, and they clearly localize the inclusion in range and cross-range.

To illustrate the statistical stability of our imaging function (5.14), we display in Figure 6.7 the histograms of the peak locations along the three coordinate axes, for one hundred realizations of the noise at 25%, 50% and 75% noise level. The effective

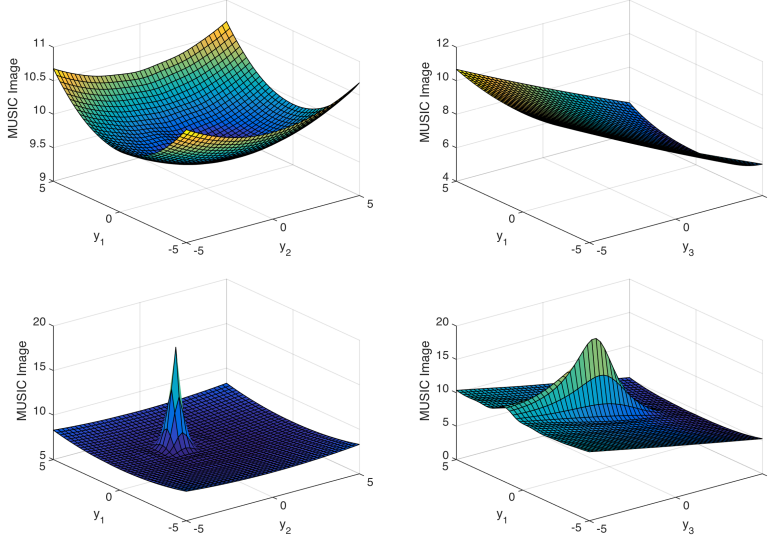


FIG. 6.5. *MUSIC imaging of one inclusion in the large aperture regime and complete measurements. We display $\mathcal{I}_{MUSIC}(\mathbf{y})$ in the plane $y_3 = L$ (left) and $y_2 = -\lambda$ (right). The axes are in units of the wavelength. The top row is for 75% noise and the bottom row for 25%.*

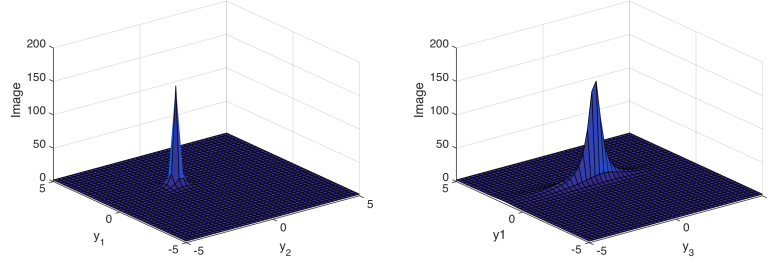


FIG. 6.6. *Imaging function (5.14) in the large aperture regime, for complete measurements and 75% noise. We display $\mathcal{I}(\mathbf{y})$ in the plane $y_3 = L$ (left) and $y_2 = -\lambda$ (right). The axes are in units of the wavelength.*

rank of the noisy data matrix $\tilde{\mathbf{D}}$ is $\tilde{\mathfrak{R}} = 1$ at 75% noise level and $\tilde{\mathfrak{R}} = 2$ for the weaker noise. We note that the focusing in cross-range is perfect for all realizations. The range focusing suffers slightly at the higher noise levels, but the error is at most 1.5λ .

Imaging is more difficult in the small aperture, as seen in Figure 6.8. Although the cross-range localization remains robust up to 50% noise, and the error is bounded by λ , which is an improvement over the resolution limit $\lambda L/a = 10\lambda$ of migration imaging, the range localization fails even at 10% noise. This is because the effective rank of $\tilde{\mathbf{D}}$ is $\tilde{\mathfrak{R}} = 2$ for all the simulations in Figure 6.8, and as explained in section 5.3.1, the projection matrices on the subspace spanned by the first two singular vectors are approximately independent of the range of the inclusion. To determine the range we need an array of larger aperture, or two arrays that view the inclusion from different directions. Alternatively, we may probe the medium with broad-band pulses and estimate the range from travel times of the scattered returns.

The histograms of the relative errors in the estimation of the reflectivity tensor

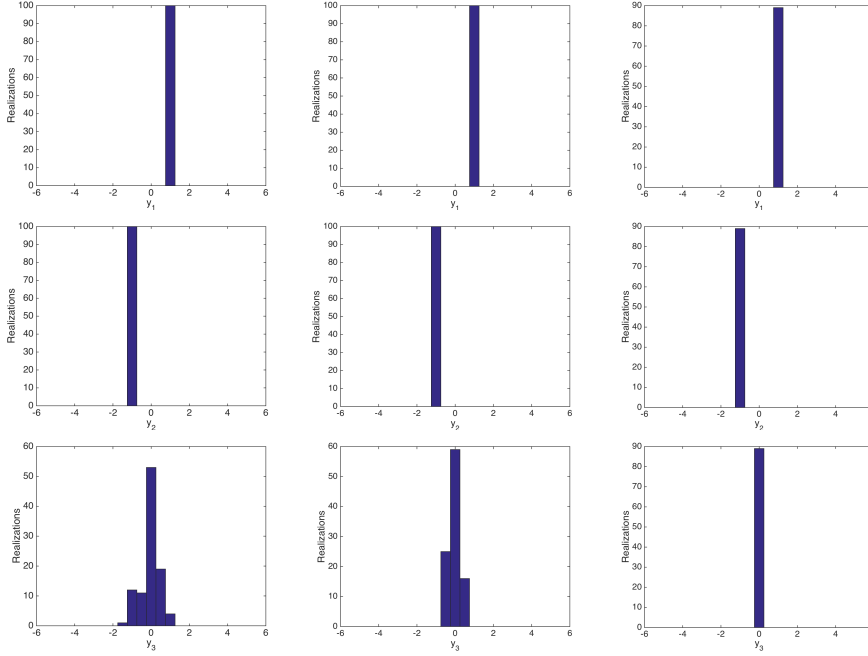


FIG. 6.7. The histograms of the peak location in y_1 (top), y_2 (middle) and y_3 (bottom) of the imaging function (5.14) in the large aperture regime. The left column is for $\sigma/\sigma_1 = 75\%$, the middle column for 50% and the right column for 25%. The abscissa is in units of the wavelength.

are displayed in Figures 6.9, for the large aperture regime and at 25% and 50% noise levels. The estimates are obtained using equations (5.25) and (5.27), and the peak location of the imaging function (5.14). The plots in the left column are for ρ_{11} , in the middle column for ρ_{33} , and in the right column for ρ_{13} . The results for ρ_{22} and ρ_{12} are similar to those for ρ_{11} , and the results for ρ_{23} are similar to those for ρ_{13} . We note that the errors are below 10% at 25% noise and naturally, they increase with the noise level. As expected, the errors are larger for ρ_{33} and ρ_{13} , but not by a big factor. This is because the condition number of the search matrix $\mathcal{G}(\vec{y})$, defined as the ratio of its largest and smallest singular values, equals 2.6 in the large aperture regime. The estimates are worse in the small aperture regime, where the condition number of $\mathcal{G}(\vec{y})$ is 23.3, as shown in Figure 6.10. Here we also have errors due to the poor estimates of the range component of the inclusion location.

6.3.2. Incomplete measurements. If the sensors measure a single component of the scattered electric field, say along \vec{e}_q , the best choice is for $q = 1$ or 2. The inversion results are very poor when $q = 3$, even at low levels of noise, as expected from the discussion in section 4.2. We show here results for the sensing matrix $\mathbf{S} = (\vec{e}_1)$, in the large aperture regime, and compare them with those in Figures 6.7 and 6.9. We do not show results in the small aperture regime because they do not add more information, and they are, as expected, worse than in the large aperture regime.

The histogram plots in Figure 6.11 show that the inclusion localization is worse than in the complete measurement case (Figure 6.7), but not dramatically so. However, the errors in the estimation of the reflectivity tensor are much larger, even at the 25% noise level. Compare the results in Figure 6.12 to those on the top row of Figure 6.9. This demonstrates the benefit of measuring more than one component of

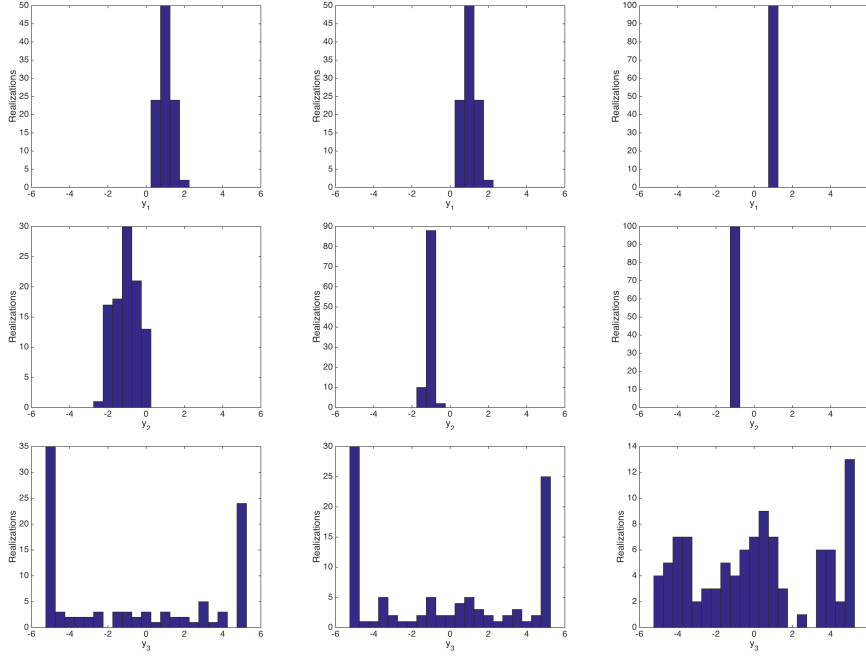


FIG. 6.8. The histograms of the peak location in y_1 (top), y_2 (middle) and y_3 (bottom) of the imaging function (5.14) in the small aperture regime. The left column is for $\sigma/\sigma_1 = 50\%$, the middle column for 25% and the right column for 10%. The abscissa is in units of the wavelength.

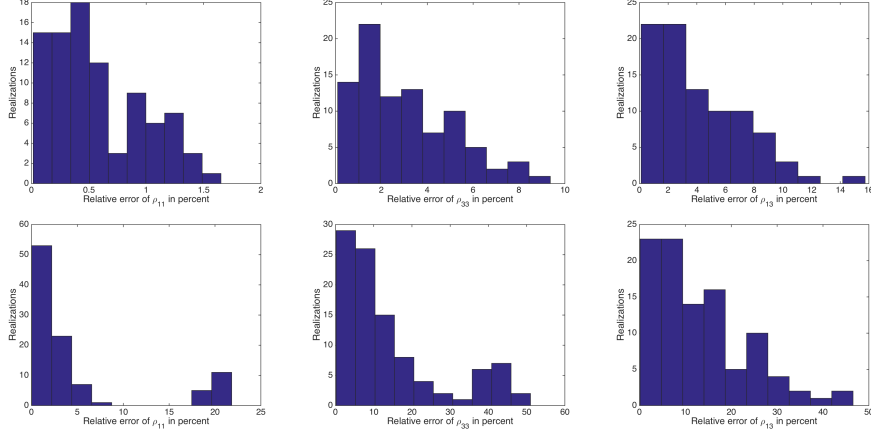


FIG. 6.9. Histograms of the relative errors of the components ρ_{11} (left), ρ_{33} (middle) and ρ_{13} (right) of the reflectivity tensor ρ , for the large aperture regime and complete measurements at 25% noise (top row) and 50% noise (bottom row). The abscissa is in percent.

the scattered electric field.

We do not display inversion results from incomplete data with the sensing matrix $\mathbf{S} = (\vec{e}_1, \vec{e}_2)$, because they are comparable to those in the complete measurements case. This is expected from the discussion in section 4.2.

6.4. Inversion results for multiple inclusions. We present results for three inclusions at $\vec{y}_1 = (\lambda, -\lambda, L)$, $\vec{y}_2 = (-10\lambda, 6\lambda, L)$ and $\vec{y}_3 = (5\lambda, 4\lambda, L)$. They are

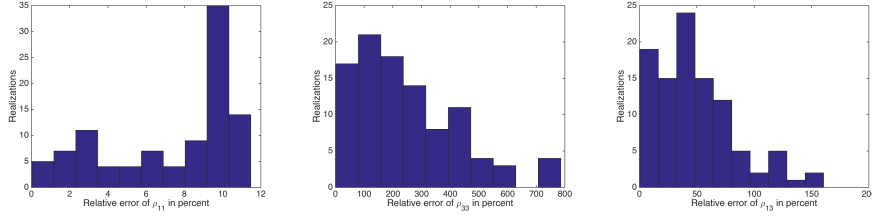


FIG. 6.10. Histograms of the relative errors of the components ρ_{11} (left), ρ_{33} (middle) and ρ_{13} (right) of the reflectivity tensor $\boldsymbol{\rho}$, for the small aperture regime and complete measurements at 25% noise. The abscissa is in percent.

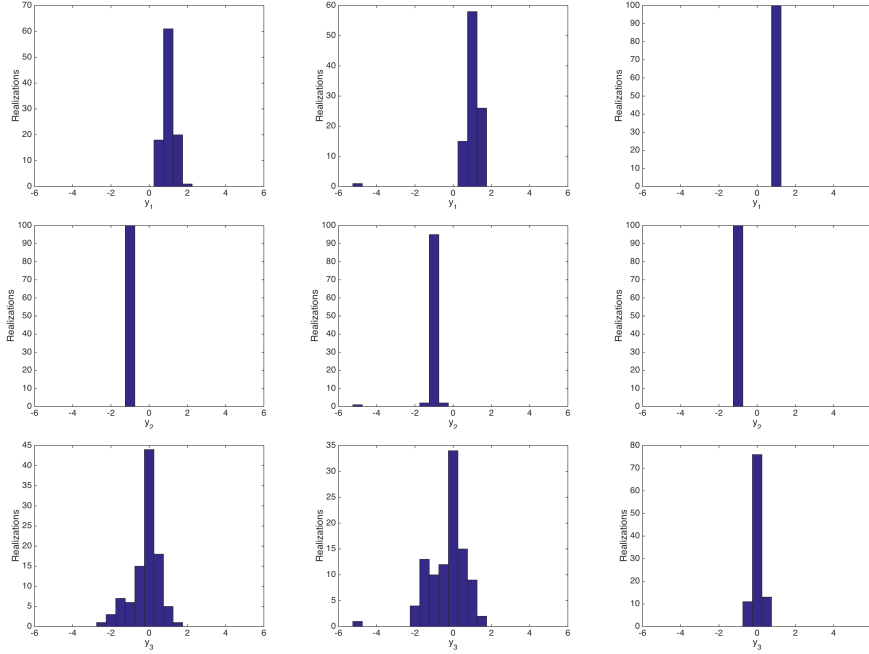


FIG. 6.11. The histograms of the peak location in y_1 (top), y_2 (middle) and y_3 (bottom) of the imaging function (5.14), in the large aperture regime, for incomplete measurements with $\mathbf{S} = (\vec{e}_1)$. The left column is for $\sigma/\sigma_1 = 75\%$, the middle column for 50% and the right column for 25%. The abscissa is in units of the wavelength.

localized using the imaging function (5.22), and their reflectivities are estimated as in (5.27). The first inclusion has the reflectivity (6.3) and for the other two we have

$$\alpha^{-3}\boldsymbol{\rho}_2 = \begin{pmatrix} 91.12 & -29.43 & -12.04 \\ -29.43 & 69.99 & -8.53 \\ -12.04 & -8.53 & 111.60 \end{pmatrix}. \quad (6.7)$$

and

$$\alpha^{-3}\boldsymbol{\rho}_3 = \begin{pmatrix} 99.37 & 5.35 & -26.89 \\ 5.35 & 101.12 & -10.37 \\ -26.89 & -10.37 & 137.06 \end{pmatrix}. \quad (6.8)$$

In the large aperture regime the matrix \mathbf{D} has rank $\Re = 9$, and singular values

$$1.76 = \sigma_1 > \sigma_2 > \dots > \sigma_5 = 1.14, \quad 0.57 = \sigma_6 > \sigma_7 > \sigma_8 = 0.18, \quad \sigma_9 = 0.07.$$

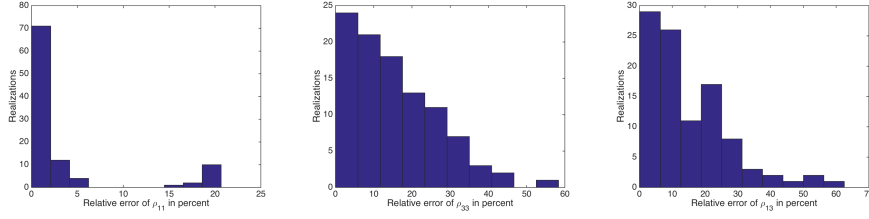


FIG. 6.12. Histograms of the relative errors of the components ρ_{11} (left), ρ_{33} (middle) and ρ_{13} (right) of the reflectivity tensor ρ , in the large aperture regime, for incomplete measurements with $\mathbf{S} = (\tilde{\mathbf{e}}_1)$ and 25% noise. The abscissa is in percent.

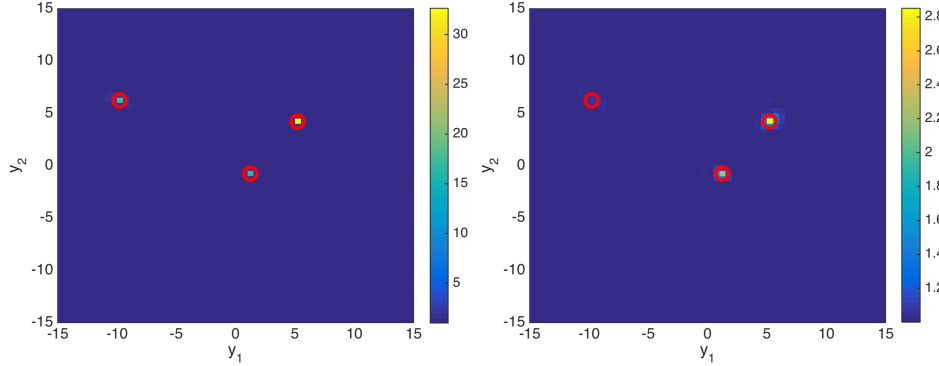


FIG. 6.13. Image of three inclusions in the large aperture regime, for complete measurements and 25% noise (left) and 75% noise (right). The display is in the plane $y_3 = L$. The axes are in units of the wavelength. The locations of the inclusions are indicated with red circles.

The rank of \mathbf{D} is still nine in the small aperture case, but the matrix has three very small singular values that are indistinguishable from noise at levels as small as 1%.

$$0.034 = \sigma_1 > \sigma_2 > \dots > \sigma_6 = 0.012, \quad 6.39 \cdot 10^{-5} = \sigma_7 > \sigma_8 > \sigma_9 = 2.12 \cdot 10^{-5}.$$

For brevity we present only results in the complete measurement case, and a few realizations of the noise. The histograms of the estimated peak locations and of the errors in the estimation of the reflectivities are similar to those in the previous section.

6.4.1. Large aperture regime. We display in Figure 6.13 the imaging function (5.22) in the plane $y_3 = L$. The image on the left is for data with 25% noise, where the effective rank of $\tilde{\mathbf{D}}$ is $\tilde{\mathfrak{R}} = 6$. The right image is for 75% noise, where the effective rank decreases to $\tilde{\mathfrak{R}} = 3$. The exact locations of the inclusions are indicated with red circles, and they coincide with the peaks of the imaging function. As expected, the peaks are more prominent when $\tilde{\mathfrak{R}}$ is closer to \mathfrak{R} i.e., for the weaker noise. Note in particular that the inclusion at $\tilde{\mathbf{y}}_2$ is barely visible at the 75% noise level, because the singular vector $\mathbf{h}_1(\tilde{\mathbf{y}}_2)$ of $\mathcal{G}(\tilde{\mathbf{y}}_2)$ has a small projection on $\text{span}\{\mathbf{u}_1, \mathbf{u}_2, \mathbf{u}_3\}$. The images in Figure 6.14 tell a similar story. They are displayed in the planes $y_2 = y_{p,2}$ for $p = 1, 2, 3$, and show that the range resolution is worse than that in cross-range, specially at the higher noise level. Moreover, consistent with Figure 6.13, the inclusion at $\tilde{\mathbf{y}}_2$ is difficult to localize at 75% noise.

We present in Table 6.4.1 the relative errors (in percent) of the estimation (5.27) of the components of the reflectivities ρ_p , for $p = 1, 2, 3$. Because the inclusions are

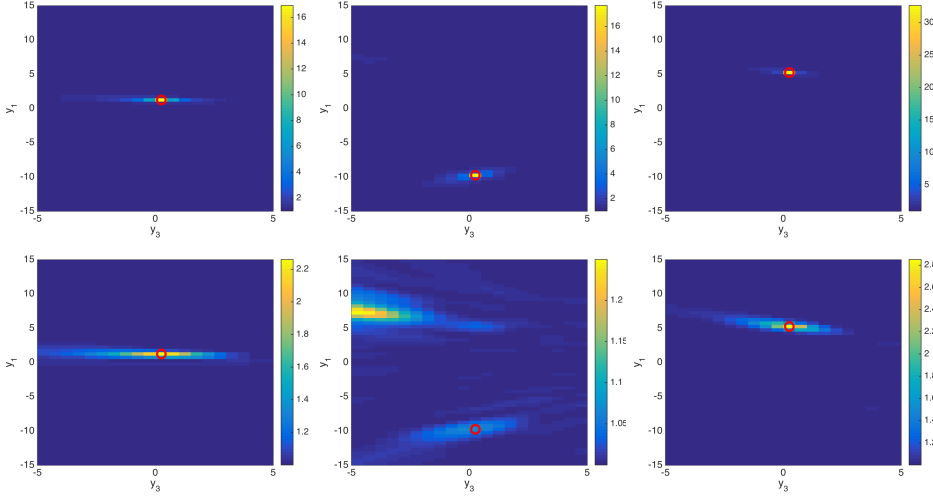


FIG. 6.14. Image of three inclusions in the large aperture regime, for complete measurements and 25% noise (top) and 75% noise (bottom). The displays are in the planes $y_2 = y_{p,2}$, for $p = 1, 2, 3$. The axes are in units of the wavelength.

		ρ_{11}	ρ_{22}	ρ_{33}	ρ_{12}	ρ_{13}	ρ_{33}
0% noise	Inclusion 1	0.01	0.02	0.1	0.03	0.06	0.08
	Inclusion 2	0.2	0.3	0.3	0.7	1.9	2.9
	Inclusion 3	0.03	0.02	0.04	0.3	0.1	0.2
25% noise	Inclusion 1	0.6	0.5	1	4.9	3.8	5.0
	Inclusion 2	3.7	5.1	2.4	10.7	19.3	44.7
	Inclusion 3	2.9	1.2	7.7	48.0	21.7	21.7
75% noise	Inclusion 1	3.3	1.8	5.7	7.1	31.3	9.9
	Inclusion 2	7.4	5.2	8.9	4.7	34.7	98.3
	Inclusion 3	2.1	0.7	7.4	45.2	18.1	49.4

TABLE 6.1

Table of relative errors (in percent) of the estimated components of the reflectivity tensors in the large aperture regime.

well localized, the errors of ρ_p are of the form (5.24), and are mostly due to the noise. The interaction between the inclusions is negligible, as seen from the very accurate results at zero noise level. This is expected because the inclusions are further apart than $\lambda L/a = \lambda$. The errors increase with the noise, but they remain small for some components, mainly on the diagonal of the reflectivity tensors.

6.4.2. Small aperture regime. As we saw in the previous section, imaging is more difficult in the small aperture regime. Range localization is impossible even at small levels of noise. Moreover, the resolution of the left image in Figure 6.15, obtained at 25% noise, is worse than that in Figure 6.13. The inclusions interact in this case, because they are separated by smaller distances than $\lambda L/a = 10\lambda$, and this adds to the difficulty. The right image in Figure 6.15 shows that one inclusion is obscured at 50% noise.

We do not show the errors in the estimation of the reflectivity tensor because they are bad even at small noise levels, due to the poor conditioning of the matrix $\Sigma(\vec{y})$ in (5.28), and the interaction of the inclusions.

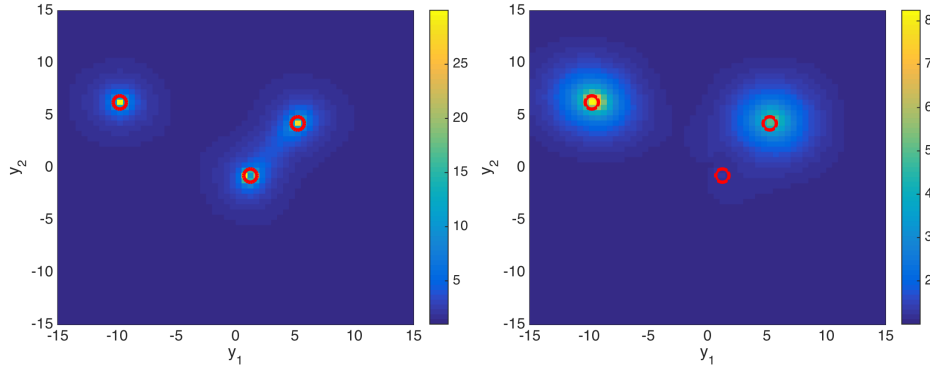


FIG. 6.15. Image of three inclusions in the large aperture regime, for complete measurements and 25% noise (left) and 50% noise (right). The display is in the plane $y_3 = L$. The axes are in units of the wavelength. The locations of the inclusions are indicated with red circles.

7. Summary. We introduced and analyzed a robust methodology for detection, localization, and characterization of small electromagnetic inclusions from measurements of the time-harmonic electric field corrupted by additive noise. The methodology is motivated by the statistical analysis of the noisy data matrix gathered by an array of sensors. In particular, it uses random matrix theory results about low rank perturbations of large random matrices. The detection of the inclusions is carried out by the inspection of the top singular values of the data matrix. The localization is done with an imaging function that uses the predictable angles between the singular vectors of the noisy data matrix and of the noiseless matrix. The characterization of the inclusions amounts to estimating their reflectivity tensor which depends on the shape of their support and their electric permittivity.

The inversion methodology is robust with respect to a significant level of additive noise, much more than standard imaging methods like MUSIC can handle. We clarify that MUSIC localization fails because the singular vectors of the noisy data matrix are not collinear to those of the unperturbed matrix. A main result of the paper is that the angles between these singular vectors can be predicted and used to obtain a robust inclusion localization. We also explain that the resolution and stability of inversion are dependent on each other, and quantify the stability gain due to larger array aperture and more than one component of the electric field being recorded and processed.

Acknowledgements. Liliana Borcea's work was partially supported by AFOSR Grant FA9550-15-1-0118.

REFERENCES

- [1] R. ALONSO, L. BORCEA, G. PAPANICOLAOU, AND C. TSOGKA, *Detection and imaging in strongly backscattering randomly layered media*, *Inverse Problems*, 27 (2011), p. 025004. [1](#)
- [2] H. AMMARI, J. GARNIER, AND V. JUGNON, *Detection, reconstruction, and characterization algorithms in wave sensor imaging*, *Discrete and Continuous Dynamical Systems – Series S*, 8 (2015), pp. 389–417. [11](#)
- [3] H. AMMARI, J. GARNIER, H. KANG, W.-K. PARK, AND K. SØLNA, *Imaging schemes for perfectly conducting cracks*, *SIAM Journal on Applied Mathematics*, 71 (2011), pp. 68–91. [1](#)
- [4] H. AMMARI, J. GARNIER, AND K. SØLNA, *A statistical approach to target detection and localization in the presence of noise*, *Waves in Random and Complex Media*, 22 (2012), pp. 40–65.

- 1
- [5] H. AMMARI, E. IAKOVLEVA, D. LESSELIER, AND G. PERRUSSON, *MUSIC-type electromagnetic imaging of a collection of small three-dimensional inclusions*, SIAM Journal on Scientific Computing, 29 (2007), pp. 674–709. [1](#), [3](#), [7](#), [11](#), [16](#)
- [6] A. AUBRY AND A. DERODE, *Detection and imaging in a random medium: A matrix method to overcome multiple scattering and aberration*, Journal of Applied Physics, 106 (2009), p. 044903. [1](#)
- [7] A. B. BAGGEROER, W. KUPERMAN, P. N. MIKHALEVSKY, ET AL., *An overview of matched field methods in ocean acoustics*, IEEE Journal of Oceanic Engineering, 18 (1993), pp. 401–424. [1](#)
- [8] J. BAIK, G. BEN AROUS, AND S. PÉCHÉ, *Phase transition of the largest eigenvalue for nonnull complex sample covariance matrices*, Annals of Probability, 33 (2005), pp. 1643–1697. [1](#), [9](#), [10](#)
- [9] J. BAIK, R. BUCKINGHAM, AND J. DiFRANCO, *Asymptotics of Tracy-Widom distributions and the total integral of a Painlevé II function*, Communications in Mathematical Physics, 280 (2008), pp. 463–497. [10](#)
- [10] F. BENAYCH-GEORGES AND R. R. NADAKUDITI, *The eigenvalues and eigenvectors of finite, low rank perturbations of large random matrices*, Advances in Mathematics, 227 (2011), pp. 494–521. [1](#), [10](#)
- [11] B. BIONDI, *3D seismic imaging*, vol. 14, Society of Exploration Geophysicists, Tulsa, 2006. [1](#)
- [12] F. CAKONI, D. COLTON, AND P. MONK, *The linear sampling method in inverse electromagnetic scattering*, vol. 80 of CBMS-NSF Regional Conference Series in Applied Mathematics, SIAM, Philadelphia, 2011. [1](#)
- [13] M. CAPITAINE, C. DONATI-MARTIN, D. FÉRAL, ET AL., *Central limit theorems for eigenvalues of deformations of Wigner matrices*, Annales de l’Institut Henri Poincaré, Probabilités et Statistiques, 48 (2012), pp. 107–133. [1](#), [9](#)
- [14] M. CHENEY AND B. BORDEN, *Fundamentals of radar imaging*, vol. 79, SIAM, Philadelphia, 2009. [1](#)
- [15] A. J. DEVANEY, *Super-resolution processing of multi-static data using time reversal and music*, tech. report, Northeastern University Report, 2000. [7](#)
- [16] A. C. FANNJIANG, *The MUSIC algorithm for sparse objects: a compressed sensing analysis*, Inverse Problems, 27 (2011), p. 035013. [1](#)
- [17] J. GARNIER AND K. SÖLNA, *Applications of random matrix theory for sensor array imaging with measurement noise*, in Random Matrix Theory, Interacting Particle Systems, and Integrable Systems, Cambridge University Press, Cambridge, 2014, pp. 223–246. [1](#), [10](#), [11](#), [19](#)
- [18] J. HADAMARD, *Résolution d’une question relative aux déterminants*, Bull. Sci. Math, 17 (1893), pp. 240–246. [5](#)
- [19] I. M. JOHNSTONE, *On the distribution of the largest eigenvalue in principal components analysis*, Annals of Statistics, 29 (2001), pp. 295–327. [9](#)
- [20] A. KIRSCH AND N. GRINBERG, *The factorization method for inverse problems*, Oxford University Press, Oxford, 2008. [1](#)
- [21] V. A. MARCHENKO AND L. A. PASTUR, *Distribution of eigenvalues for some sets of random matrices*, Matematicheskii Sbornik, 114 (1967), pp. 507–536. [1](#), [9](#)
- [22] R. O. SCHMIDT, *Multiple emitter location and signal parameter estimation*, IEEE Transactions on Antennas and Propagation, 34 (1986), pp. 276–280. [1](#)
- [23] A. SIHVOLA AND I. LINDELL, *Polarizability modeling of heterogeneous media*, Progress in Electromagnetics Research (PIER 6), Dielectric Properties of Heterogeneous Materials, Priou, A.(ed.), Elsevier, Amsterdam, (1992). <http://www.jpier.org/PIER/pier06/03.900105.pdf>. [16](#)